UC Berkeley
UC Berkeley Previously Published Works

Title

Sedimentary reservoir oxidation during geologic CO2 sequestration

Permalink

https://escholarship.org/uc/item/4465z1ph

Authors

Lammers, Laura N
Brown, Gordon E
Bird, Dennis K
et al.

Publication Date

2015-04-01

DOI

10.1016/j.gca.2015.02.001

Peer reviewed

Sedimentary reservoir oxidation during geologic CO$_2$ sequestration

Laura N.Lammers[a], Gordon E.Brown Jr.[a,b], Dennis K.Bird[a], Randal B.Thomas[c], Natalie C.Johnson[a], Robert J.Rosenbauer[c], KatharineMaher[a]

[a] Dept. of Geological & Environmental Sciences, Stanford University, Stanford, CA, 94305-2115, United States

[b] Dept. of Photon Science, SLAC National Accelerator Laboratory, Stanford University, Menlo Park, CA 94025, United States

[c] United States Geological Survey, Menlo Park, CA, 94025, United States

Abstract

Injection of carbon dioxide into subsurface geologic reservoirs during geologic carbon sequestration (GCS) introduces an oxidizing supercritical CO$_2$ phase into a subsurface geologic environment that is typically reducing. The resulting redox disequilibrium provides the chemical potential for the reduction of CO$_2$ to lower free energy organic species. However, redox reactions involving carbon typically require the presence of a catalyst. Iron oxide minerals, including magnetite, are known to catalyze oxidation and reduction reactions of C-bearing species. If the redox conditions in the reservoir are modified by redox transformations involving CO$_2$, such changes could also affect mineral stability, leading to dissolution and precipitation reactions and alteration of the long-term fate of CO$_2$ in GCS reservoirs. We present experimental evidence that reservoirs with reducing redox conditions are favorable environments for the relatively rapid abiotic reduction of CO$_2$ to organic molecules. In these experiments, an aqueous suspension of magnetite nanoparticles was reacted with supercritical CO$_2$ under pressure and temperature conditions relevant to GCS in sedimentary reservoirs (95–210 °C and ~100 bars of CO$_2$). Hydrogen production was observed in several experiments, likely caused by Fe(II) oxidation either at the surface of magnetite or in the aqueous phase. Heating of the Fe(II)-rich system resulted in elevated P_{H2} and conditions favorable for the reduction of CO$_2$ to acetic acid. Implications of these results for the long-term fate of CO$_2$ in field-scale systems were explored using reaction path modeling of CO$_2$ injection into reservoirs containing Fe(II)-bearing primary silicate minerals, with kinetic parameters for CO$_2$ reduction obtained experimentally. The results of these calculations suggest that the reaction of CO$_2$ with reservoir constituents will occur in two primary stages (1) equilibration of CO$_2$ with organic acids resulting in mineral–fluid disequilibrium, and (2) gradual dissolution of primary minerals promoting significant CO$_2$ reduction through the release of Fe(II). The reduction of CO$_2$ is identified as a new trapping mechanism that could significantly enhance the long-term stability of GCS reservoirs. Identification of reservoir characteristics that promote CO$_2$ redox transformations could be used as an additional factor in screening geologic reservoirs for GCS.

1. Introduction

The sequestration of industrial carbon dioxide emissions into geologic formations is considered a viable strategy to mitigate the rise in atmospheric CO_2 (cf. Xu et al., 2004, Benson and Cole, 2008, Bickle, 2009). The fate of injected CO_2 depends on physiochemical interactions with reservoir mineral and fluid phases, which control the long-term stability of geologic carbon sequestration (GCS) reservoirs (Hitchon, 1996). Geologic reservoirs in sedimentary rocks currently being considered for GCS contain complex assemblages of detrital and authigenic minerals, saline aqueous solutions, and variable amounts of liquid, gaseous, and solid hydrocarbons. Geochemical investigations into the fate of CO_2 in these reservoirs have focused on three primary trapping mechanisms, including (1) capillary trapping of CO_2 bubbles in constricted pores, (2) solubility trapping of CO_2 dissolved into the aqueous brine, and (3) carbonate mineralization, including magnesite, calcite, and siderite formation (Xu et al., 2004, Benson and Cole, 2008). A fourth possible fate is conversion of CO_2 to more reduced hydrocarbon or organic acid molecules via redox reactions. Carbon dioxide reduction to organic molecules can be catalyzed by Fe-oxide minerals such as magnetite (McCollom and Seewald, 2007, Luquot et al., 2012), which are common in sedimentary formations. Extensive CO_2 reduction in sedimentary reservoirs would affect the stability of detrital and authigenic Fe(II)-silicate and -sulfide minerals, which in turn could modify reservoir porosity, permeability, trace element release, and ultimately the fate of sequestered CO_2.

Transition metal and metal oxide mineral surfaces are known to catalyze the reduction of inorganic carbon to more reduced hydrocarbon molecules and even to graphite. The most widely recognized mechanism of abiotic carbon reduction and hydrocarbon generation is known as Fischer–Tropsch synthesis (FTS), for which a general reaction can be written:

$$n\mathrm{CO} + (2n+1)\mathrm{H}_2 \rightarrow \mathrm{C}_n\mathrm{H}_{2n+2} + n\mathrm{H}_2\mathrm{O}. \qquad (1)$$
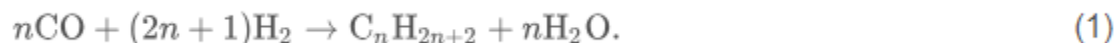
Gas-phase reduction of CO_2 to form CO in reaction 1 is commonly catalyzed by magnetite (e.g., Grenoble and Estadt, 1981):

$$\mathrm{CO}_2 + \mathrm{H}_2 \rightarrow \mathrm{CO} + \mathrm{H}_2\mathrm{O}. \qquad (2)$$

Numerous experimental and computational efforts have been directed toward identifying and optimizing key FTS catalysis mechanisms on the surfaces of transition metals and metal oxides (Niemantsverdriet and van der Kraan, 1980, Dictor and Bell, 1986, Van Der Laan and Beenackers, 1999, de Smit and Weckhuysen, 2008, Gracia et al., 2009, Huo et al., 2009, Zhuo et al., 2009, Marshall and Medlin, 2011, Thüne et al., 2012). Despite these efforts, the conditions under which FTS reactions can occur remain poorly constrained.

The abiotic synthesis of reduced carbon species including organic acids, hydrocarbons, and graphite has been inferred from multiple geologic settings such as meteorites (Schulte and Shock, 2004), hydrothermal systems (Shock, 1990, Shock, 1995, Shock and Schulte, 1998, Horita and Berndt, 1999, McCollom and Seewald, 2006, Fu et al., 2007, Shock et al., 2013), and Earth's mantle (McCollom and Seewald, 2001, Schulte et al., 2006). Prior determinations of the thermodynamic stability of numerous organic molecules (Shock and Helgeson, 1990, Schulte and

Shock, 1993, Shock, 1995) have enabled calculations of the chemical affinity of postulated abiotic organic synthesis reactions arising from fluid mixing in real hydrothermal systems (Shock and Canovas, 2010). Several studies have attempted to duplicate the geochemical conditions leading to abiotic carbon reduction using hydrothermal reactors, producing carboxylic acids (Chen and Bahnemann, 2000, McCollom and Seewald, 2003a), complex organic molecules (Williams et al., 2011), and amorphous carbon associated with nanoparticulate magnetite (Luquot et al., 2012). Both experiments and thermodynamic calculations have improved our understanding of the processes controlling abiotic transformations of organic matter. Such transformations are thought to be catalyzed by the surfaces of naturally occurring minerals, including clays and magnetite (Palmer and Drummond, 1986, Shock, 1995). In fact, the magnetite surface is known to participate in other geochemically significant redox reactions, such as reduction of Cr(VI) in contaminated groundwater (Peterson et al., 1996).

Studies of petroleum reservoirs suggest that redox reactions among inorganic carbon (IC) and organic carbon (OC) species likely control the redox environment of relatively low-T reservoirs (Helgeson et al., 1993). Organic acid anions are a major constituent of oilfield brines (Kharaka et al., 1977), and the assumption of metastable equilibrium among organic acids and IC species has been used in the past as an indicator of reservoir hydrogen fugacity (cf. Shock, 1988, Helgeson et al., 1993). Metastable equilibrium occurs when a subset of phases or species obtains chemical equilibrium but is not necessarily chemically equilibrated with other phases or species in the system. In oilfield brines, the aqueous hydrogen activity is constrained by the metastable reaction between carbon dioxide and acetic acid (CH_3COOH):

$$2CO_2(g) + 4H_2(aq) \leftrightarrow CH_3COOH(aq) + 2H_2O(l), \qquad (3)$$
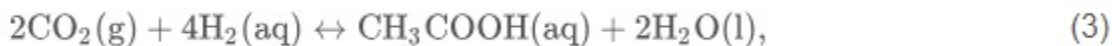
where "g" and "aq" denote gas and aqueous species, respectively, and "l" denotes the liquid solvent. True equilibrium between aqueous CO_2 and H_2 would result in the formation of methane, but methane equilibration with CO_2 is extremely slow, requiring $>10^5$ years at temperatures $<300\ °C$ (Giggenbach, 1987, Shock, 1990). The lowest temperature of isotopic equilibration between CH_4 and CO_2 in hydrothermal settings is 320 °C (Shock, 1990), which is significantly higher than typical reservoirs considered for GCS. The activity of $H_2(aq)$, a_{H_2}, can be determined from the equilibrium constant (K) for reaction 3, and the fugacity of CO_2 and activity of acetic acid (f_{CO_2} and a_{Ac}, respectively) assuming unit activity of water:

$$\log(a_{H_2}) = \tfrac{1}{4}(\log(a_{Ac}) - 2\ \log(f_{CO_2}) - \log(K)). \qquad (4)$$

We note that the activity and fugacity of hydrogen are among a number of thermodynamic variables (e.g., $a_{H_2}, f_{H_2}, a_{O_2}, f_{O_2}$, and pe) that can be used to describe the redox environment and that are related by established equilibria between the liquid and gas or supercritical fluid phases. Helgeson et al. (1993) calculated the f_{O_2} of oilfield waters as a function of temperature, assuming metastable equilibrium among IC and OC species. The authors found minimal deviation from the curve represented by Eq. (4), which was interpreted as evidence that the fluid hydrogen activity of natural

geologic reservoirs is controlled by metastable equilibrium among organic and inorganic carbon species (Fig. 1). We have plotted the temperature dependence of Eq. (4) in Fig. 1 assuming an a_{Ac} = 0.23 and an f_{CO_2} =10-4, which are non-unique values consistent with the range of organic acid concentrations observed in sedimentary petroleum reservoirs (Helgeson et al., 1993).
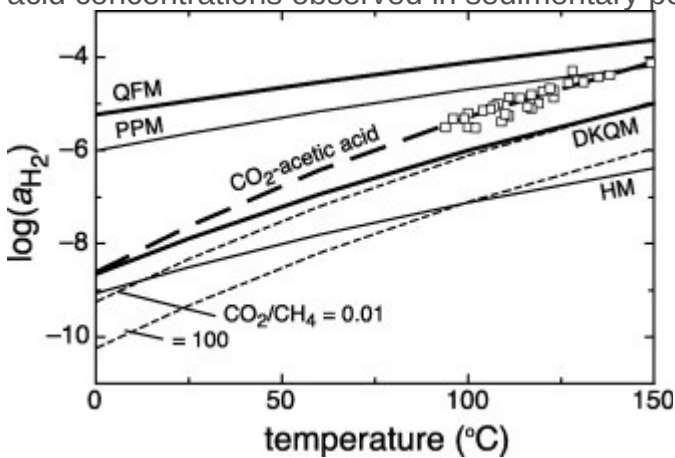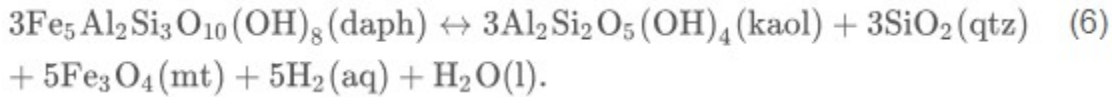

Download high-res image (172KB)

Download full-size image

Fig. 1. Calculated aqueous hydrogen activity as a function of temperature for Gulf Coast petroleum reservoirs (open boxes; Helgeson et al., 1993), with theoretical redox buffer curves including the quartz–fayalite–magnetite (QFM), daphnite–kaolinite–quartz–magnetite (DKQM), pyrite–pyrrhotite–magnetite (PPM), and hematite–magnetite (HM) mineral buffers plotted for reference. The thick dashed line indicates equilibrium between CO2 and acetic acid, calculated using Eq. (4) assuming acetic acid activity = 0.023 and $f_{CO_2} = 10^{-4}$ (see text for details). The lower dashed lines indicate the thermodynamic equilibrium ratios of carbon dioxide to methane fugacities calculated for a given hydrogen activity and temperature. The DKQM and QFM buffers bracket a range of hydrogen activities expected to be relevant to GCS reservoirs.

In contrast, studies of high-T hydrothermal and metamorphic fluids suggest that mineral assemblages containing redox-active species such as Fe(II) may control the redox environment (cf. Shock, 1990). Equilibrium between the minerals quartz (qtz), fayalite (fa), and magnetite (mt) is often used to represent the theoretical redox conditions in basaltic hydrothermal systems (Haggerty, 1978). This QFM assemblage constrains the activity of aqueous hydrogen through the oxidation of Fe(II) in fayalite to form mixed-valent magnetite,

$$3\mathrm{Fe_2SiO_4(fa)} + 2\mathrm{H_2O(l)} \leftrightarrow 2\mathrm{Fe_3O_4(mt)} + 3\mathrm{SiO_2(qtz)} + 2\mathrm{H_2(aq)}. \qquad (5)$$
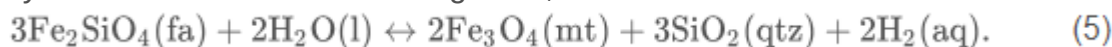
Most reservoirs currently targeted for GCS do not contain a significant fraction of the Fe(II)-bearing primary mineral fayalite, but many sedimentary reservoirs do contain detrital and/or diagenetic Fe(II)-bearing chlorite and smectite (Ryan and Reynolds, 1996, Krevor et al., 2012, Lu et al., 2012). For example, chlorite is a significant component of the Tuscaloosa formation, which is the target reservoir for the Cranfield CO_2 injection site in Mississippi, U.S.A. Complex chlorite/smectite clays are represented here by the Fe(II) end-member corresponding stoichiometrically to daphnite (Helgeson et al., 1978), which is often referred to interchangeably as chamosite. In this case, the redox control can be described as equilibrium between daphnite (daph), and secondary kaolinite (kaol), quartz, and

magnetite (i.e., DKQM). The DKQM assemblage produces H_2 through the oxidation of Fe(II) in daphnite,

$$3Fe_5 Al_2 Si_3 O_{10}(OH)_8 (daph) \leftrightarrow 3Al_2 Si_2 O_5 (OH)_4 (kaol) + 3SiO_2 (qtz) \quad (6)$$
$$+ 5Fe_3 O_4 (mt) + 5H_2 (aq) + H_2 O(l).$$

The production of hydrogen in both assemblages is associated with the oxidation of Fe(II) to Fe(III) to form magnetite and can be expressed as the net reaction ([Mayhew et al., 2013](#)):

$$3Fe^{2+}(aq) + 4H_2 O(l) \rightarrow Fe_3 O_4 (mt) + H_2 (aq) + 6H^+ (aq). \quad (7)$$
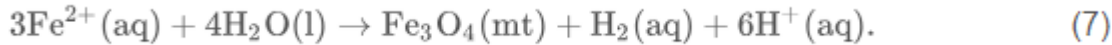
Equilibrium values of a_{H_2} can be calculated from $\log(K)$ of reactions 5 and 6 at a given temperature and pressure, assuming unit activity of water and mineral phases and pure phase thermodynamic data reported in [Helgeson et al. (1978)](#). A comparison of the theoretical equilibrium a_{H_2} as a function of temperature for QFM, DKQM, and CO_2-acetic acid is depicted in [Fig. 1](#). Daphnite is not a stoichiometric phase in typical [sedimentary basins](#) but rather the Fe(II) end-member of the [solid solution](#) with clinochlore ($Mg_5Al_2Si_3O_{10}(OH)_2$).

Diagenetic and sedimentary chlorite and smectite can contain a significant fraction of Fe(II). For example, the Ladbroke Grove–Katnook reservoir, which has been used as a [natural analog](#) for GCS ([Watson et al., 2004](#)), contains an Fe(II)-chlorite with an intermediate composition of $Fe_3Mg_2Al_2Si_3O_{10}(OH)_8$ ([Luquot et al., 2012](#)). The equilibration of this solid solution with kaolinite, quartz, and magnetite would yield a curve offset from the DKQM curve in [Fig. 1](#) toward lower a_{H_2}. Curves representing the common hydrothermal mineral buffer assemblages hematite–magnetite (HM) and pyrite–pyrrhotite–magnetite (PPM) are also shown in [Fig. 1](#) for reference. The QFM and DKQM mineral assemblages (i.e., reactions 5 and 6) appear to bracket the range of redox conditions in natural sedimentary basins. The redox state in this range of a_{H_2} is sufficiently reducing such that the CO_2:CH_4 ratio at [thermodynamic equilibrium](#) is much less than one, which indicates that CO_2 reduction to organic species is thermodynamically favorable.

We performed both hydrothermal experiments and reaction path calculations to evaluate the short-term (i.e., from injection to 10^3 year) and long-term (i.e., 10^3–10^6 year) fate of CO_2 during GCS. Experiments were conducted in a hydrothermal reaction cell ([Rosenbauer et al., 2005](#), [Johnson et al., 2014](#)) to constrain the kinetics of CO_2 conversion to acetic acid (i.e., reaction 3) at the relatively low-temperatures and high-pressures associated with GCS reservoirs, and in the presence of a mineral known to catalyze CO_2 reduction, nanoparticulate magnetite. Aqueous acetic acid concentrations were observed to increase during the experiments, and corresponding calculations of the chemical affinity of reaction 3 confirm that reduction of carbon dioxide to acetic acid was thermodynamically favorable under the experimental conditions. Results of these experiments support the conclusion that reduction of CO_2 to organic acids, specifically acetic acid, occurs in the presence of magnetite. Geochemical modeling was performed to evaluate the impact of CO_2 reduction on both the short- and long-term fate of CO_2 during GCS, using the rate constant for acetic acid formation from CO_2 obtained experimentally. These calculations simulate the evolution of hypothetical reservoirs containing primary

Fe(II)-bearing silicates including fayalite and daphnite. The QFM and DKQM phase assemblages were selected for reaction path calculations, because they are commonly considered to buffer the redox environment of reservoir fluid in the range observed in natural sedimentary basins. Results of these calculations suggest that extensive CO_2 injection will initially lead to an abrupt decrease in a_{H_2} due to metastable equilibration among IC and OC species lasting ~10^3 years. Over long (i.e., 10^6 year) timescales, fluid re-equilibration with the solid mineral assemblage will allow for more extensive conversion of CO_2 to organic carbon, leading to organic trapping. The mineralogic changes resulting from CO_2 injection and reservoir mineral oxidation will in turn alter the reservoir and caprock properties and therefore the efficacy of CO_2 storage. Oxidation–reduction reactions should be considered in comprehensive investigations assessing the evolution and fate of CO_2 during GCS.

2. Methods

2.1. Hydrothermal experiments

Carbon dioxide reduction experiments were performed in a flexible gold-bag reaction cell housed in a steel pressure vessel containing water as the pressurizing fluid (Seyfried et al., 1987, Rosenbauer et al., 2005, Johnson et al., 2014). Details of the apparatus can be found in Seyfried et al. (1979), and the modifications required for high pressure CO_2 injection are described in Rosenbauer et al. (2005) and Johnson et al. (2014). Six experiments were completed in which a suspension of magnetite nanoparticles was sealed inside a gold bag reaction cell using a titanium head assembly and subsequently pressurized with CO_2 (Table 1). Briefly, CO_2 was added to the gold bag using a high-pressure syringe pump. Prior to filling the headspace with CO_2, the gold bag was flushed three times with CO_2 at 40 bars to purge atmospheric O_2. An aliquot of $H_2(g)$ was injected into the flushed headspace at 1 bar to ensure that the initial system would be close to redox equilibrium. The initial mole fraction of H_2 was measured for all experiments except Exp. 6, and the values are reported in Table 1. The bag was then filled to a PCO_2 between 40 and 55 bars to obtain a PCO_2 of ~100 bars at temperature (Table 2). The initial volume of the vessel was approximately 200 mL, and the initial volume of the aqueous suspension ranged from 55 to 153 mL. The compositions of both the aqueous and supercritical CO_2 phases at the beginning of each experiment are listed in Table 1. Care was taken to ensure that no catalytic surfaces were exposed in the reaction cell. A non-reactive TiO_2 layer was formed on the surface of the Ti head by baking the entire gold bag assembly in air at 450 °C for several days prior to each experiment. This procedure also ensured the removal of contaminant carbon from the reaction cell.

Table 1. Initial compositions of the hydrothermal reaction cell for experiments and blanks. The Fe(II) and Fe(III) s./aq. columns indicate the total moles of each species added during suspension preparation and magnetite synthesis, that subsequently partitioned between the solid (s.) and aqueous (aq.) phases calculated from reagent masses.

Experiment	T(°C)	P(bars)	Fe(II) s./aq. (moles × 10³)	Fe(III) s./aq. (moles × 10³)	NaCl aq. (M)	Fluid volume (mL)	Vol. Rxn. cell (mL)	Vol. head space (mL)	Moles CO_2	xH_2(×10⁶)
Exp. 1	20	57	5.02	10.0	0.73	55.0	198	143	0.53	161
Exp. 2	22	80	15.0	36.9	0.92	153	211	58.0	1.06	286
Exp. 3	21	57	9.73	22.2	0.82	106	211	106	0.39	6.88
Exp. 4	20.7	40	10.5	20.6	0.81	102	186	83.7	0.18	b.d.
Exp. 5	20.6	48	10.4	20.1	0.79	103	219	116	0.34	3982
Exp. 6	18	38	10.1	19.9	0.96	83.4	225	141	0.30	n.a.
Blank 1	25	100	–	–	–	–	190	190	3.53	n.a.
Blank 2	20	57	–	–	–	–	190	190	0.70	n.a.
Blank 3	20	1	10.1	20.0	0.85	94.7	220	125	–	n.a.

b.d. = below detection.

n.a. = not analyzed.

Table 2. Summary of P–T conditions, gas phase compositions and acetic acid ("Ac") concentrations throughout the hydrothermal experiments. All experiments were performed in the presence of an aqueous suspension of magnetite particles with pressurized CO_2 added to the headspace. Uncertainty on the hydrogen activity calculated through propagation of error does not exceed 3×10^{-5}. Chemical affinity "A" is calculated using Eq. (10) for acetic acid formation from CO_2 as expressed in reaction 3.

Sample	Time (h)	Measured					Calculated		
		T(°C)	P(bar)	$[H_2]$ (ppm)	PH2(mbar)	Log[Ac] (M)	Log(f_{CO_2})	Log(a_{H_2})	A(kcal/mol)
Exp. 1-1	0	20.3	57	161.0	9.18	b.d.	1.60	−4.61	–
Exp. 1-2	45	96.8	129	1050	135	b.d.	1.94	−3.74	–
Exp. 1-3	90	96.8	109	1281	140	b.d.	1.89	−3.77	–
Exp. 1-4	162	97.8	103	1542	159	−5.13	1.88	−3.73	858.6
Exp.2-1	0	29.4	89	286.3		b.d.	1.65	−4.40	
Exp. 2-2	23	44.7	157	229.7	36.1	b.d.	1.83	−3.92	–
Exp. 2-3	67	142.7	261	241.1	62.9	b.d.	2.19	−4.01	–
Exp. 2-4	143	72.8	62	185.5	11.5	−5.18	1.69	−4.94	643.0
Exp. 2-5	383	41.0	32	202.0	6.5	−5.24	1.44	−5.23	730.4

Sample	Time (h)	Measured					Calculated		
		T(°C)	P(bar)	$[H_2]$ (ppm)	PH2(mbar)	Log[Ac] (M)	Log(f_{CO_2})	Log(a_{H_2})	A(kcal/mol)
Exp. 2-6	407	20.0	1	b.d.	b.d.	b.d.	b.d.	b.d.	–
Exp.3-1	0	20.0	57	6.881		b.d.	1.60	−5.98	
Exp. 3-2	16	101.2	168	57.81	9.7	b.d.	2.01	−4.81	–
Exp. 3-3	67	110.9	94	850.1	79.9	−5.62	1.86	−4.06	714.8
Exp. 3-4	163	110.8	89	829.8	73.9	−5.32	1.84	−4.10	677.4
Exp. 3-5	331	25.6	16	803.5	12.9	b.d.	1.17	−4.95	–
Exp.4-1	0	20.4	40	10.00		−4.93	1.50	−6.37	
Exp. 4-2	17	98.6	116	240.6	27.9	−5.86	1.91	−4.46	697.6
Exp. 4-3	25	149.5	114	407.4	46.4	−5.14	1.94	−4.24	378.8
Exp. 4-4	44	149.4	107	1461	156	b.d.	1.91	−3.72	–
Exp. 4-5	100	143.2	88	b.d.	b.d.	−5.16	1.84	b.d.	–
Exp. 4-6	191	155.8	97	1929	186	−4.81	1.87	−3.65	497.6
Exp. 4-7	308	151.3	85	2084	177	−4.69	1.82	−3.68	497.5
Exp. 4-8	385	150.3	80	1342	107	−4.62	1.79	−3.91	416.4
Exp. 4-9	477	148.2	77	51.30	4.0	−4.36	1.78	−5.35	−76.1
Exp. 5-1	0	20.6	48	3982		−5.62	1.56	−3.65	
Exp. 5-1	0	22.0	48	3982	191	−5.62	1.56	−3.65	1241.2
Exp. 5-2	16	200.0	245	2918	715	−4.64	2.18	−2.89	535.5
Exp. 5-3	24	184.6	159	2859	455	b.d.	2.05	−3.16	–
Exp. 5-4	93	218.3	178	1.812	0.3	−4.18	2.06	−6.20	−932.6
Exp. 5-5	258	214.9	155	b.d.	b.d.	−4.02	2.02	b.d.	–
Exp. 6-0	0	18.00	38	b.d.	b.d.	−5.68	1.48	b.d.	–

Sample	Time (h)	Measured					Calculated		
		$T(°C)$	P(bar)	[H$_2$] (ppm)	PH2(mbar)	Log[Ac] (M)	Log(f_{CO_2})	Log(a_{H_2})	A(kcal/mol)
1									
Exp. 6-2	144	176.1	114	1543	176	−4.97	1.93	−3.62	400.1
Exp. 6-3	336	173.8	100	301.6	30.2	−4.60	1.90	−4.40	99.7
Exp. 6-4	504	183.7	90	b.d.	b.d.	b.d.	1.82	b.d.	–

During the experiments, the entire apparatus was allowed to rock continuously to ±180° to ensure a well-mixed fluid phase. Fluids were sampled periodically via a titanium capillary tube accessed through a high-pressure steel metering valve. The inlet to the capillary was fitted with a gold wire filter at the beginning of each experiment to prevent solids loss during sample collection. Fluids were collected in an airtight syringe triply purged with N$_2$. Supercritical fluid samples were collected by opening the sample valve with the system upright, while aqueous samples were collected by opening the valve with the system inverted. Whole samples of the aqueous phase were immediately frozen after collection to inhibit biological activity. Samples of the supercritical CO$_2$ phase were refrigerated to minimize H$_2$ loss by diffusion. The final sample aliquot in each experiment was taken after cooling the system overnight. It was not possible to obtain reliable measurements of aqueous Fe speciation or total Fe concentration using this sampling technique, due to the abrupt decrease in PCO$_2$ in the fluid capillary and the rapid oxidation of Fe in the syringe during sample collection. Future studies should develop techniques to precisely measure both the concentration and speciation of aqueous Fe.
In some experiments (i.e., 3 and 4), the internal pressure was allowed to decrease upon sampling, while in others (i.e., 1 and 6), the pressure was maintained by pumping additional water into the pressure fluid reservoir. Pressures and temperatures were recorded at every sampling, so PCO$_2$ is known even in variable-P experiments (Table 2). Temperatures were measured with a thermocouple inserted into the pressure fluid reservoir, and pressures were measured through a transducer connected to the same reservoir. The system temperature was regulated using a temperature controller linked to the thermocouple that controlled a heating coil embedded in the hydrothermal apparatus. The temperature variability during heating typically did not exceed ±10 °C. However, instabilities in the thermocouple controller caused temperature shifts during Exp. 2, so it is not possible to determine the average T of this experiment. Experiment 2 is included in the analysis here despite T instability, because it provides an additional constraint on the relationship between PH$_2$ and temperature. We estimate the uncertainties of the pressure and temperature measurements obtained at the time of sample collection to be ±2 bars and ±1 °C.

2.1.1. Magnetite synthesis

Magnetite nanoparticles were synthesized using the aqueous co-precipitationof Fe(II) and Fe(III) chloride salts (Morin et al., 2009). Briefly, 1 M solutions of Fe(II) and Fe(III) chloride salts dissolved in degassed, deionized 18 MΩ water were mixed at a 1:2 ratio in an anaerobic glovebox with a 5% H$_2$,

95% N_2 atmosphere. The pH of the fluid was raised to a value of 7.0 ± 0.1 through the addition of N_2-purged 1 N NaOH solution. To minimize both Fe oxidation and carbon contamination, magnetite nanocrystals were freshly synthesized prior to each experiment. Initial suspension compositions used in each experiment are reported in Table 1. The resulting suspension contained magnetite nanoparticles suspended in a ~0.8 M NaCl brine. Although the entire suspension including both magnetite and brine was transferred as quickly as possible to the hydrothermal reactor apparatus, the setup procedure could take up to 6 h, during which time the suspension was exposed to air. Synthesized magnetite nanoparticles were examined using an FEI Technai G2 F20 X-TWIN transmission electron microscope (TEM). The magnetite grains were approximately 40 nm in diameter and exhibited an octahedral morphology consistent with the exposure of the Fe_3O_4 (1 1 1) face. The estimated specific surface area of the dry solid is approximately 30 m^2/g assuming a homogeneous particle size distribution. Powder X-ray diffraction (XRD) was performed on a Rigaku X-ray Diffractometer, model number CM2029 using monochromated Cu Kα radiation at 2-theta values ranging between 10° and 70° to determine Fe-oxide mineralogy, and the results of both XRD and TEM are available in the Supplementary Materials.

2.1.2. Sample analysis

Several analyses were routinely performed on fluid and supercritical-phase samples. Aqueous fluid samples were analyzed using a Dionex DX500 ion chromatograph to identify and quantify organic acid anions in the aqueous phase. Organic acid anions in the mixed calibration solution included acetate, citrate, formate, glycolate, lactate, oxalate, and succinate, although only acetate, formate, and occasionally glycolate were detectable in our samples. Samples were introduced into the instrument via a 50 μL sample loop at a total flow rate of 1 mL/min. Acids were separated on a Dionex ICE-AS6 column, with a 0.8 mM heptafluorobutyric acid (HPFA) eluent diluted 1:1 with water. All fluids were degassed for 30 min with N_2 prior to use. A 5 mM tetra butyl ammonium hydroxide regenerant solution was used for the AMMS suppressor. Analytical uncertainties on the concentration of measured formic and acetic acids are approximately 10% relative standard deviation (RSD) based on replicate analyses of a standard. The detection limit for acetate was approximately 0.09 ppm (log[Ac] = −5.88) based on the lowest quantifiable value. It is possible that some amount of acetic acid partitioned into the sc-CO_2 phase (Burant et al., 2013), and as such our aqueous measurements may represent a minimum conversion rate.

Gases collected from the supercritical fluid phase were analyzed using gas chromatography (GC) to measure the concentration of hydrogen. Isothermal (30 °C) analyses were performed using headspace injections via a gas sample loop on an Agilent 6890 Series Gas Chromatograph with a pulse discharge detector. An Agilent J&W Molesieve-5A capillary column was used with a He carrier gas and a nominal flow rate of 1.5 mL/min. This column was used to remove carbon dioxide from the gas phase. Integration of peak areas was performed using Agilent ChemStation software. The hydrogen concentration was quantified based on a 4-point calibration curve ranging in concentration from 100 to 10,000 ppm H_2. Uncertainties in individual analyses are reported as the error on a linear

regression of the calibration curve, which equates to an analytical precision of ±66 ppm H_2. This magnitude of uncertainty is considerably larger than the estimated standard error (s.e.) on replicate analyses of the standard. The maximum magnitude of uncertainties on H_2 activity and fugacity were determined by propagating errors on pressure and hydrogen concentrations.

Carbon isotopes were measured to determine the fraction of total organic carbon (TOC) in the experimental fluids derived from the injected CO_2. Selected samples were analyzed for TOC concentration and $\delta^{13}C_{TOC}$ using cavity ring-down spectroscopy (CRDS). Briefly, 12 mL sample aliquots were passed through Dionex OnGuard Ag ion exchange cartridges to extract Cl^-, which interferes with the isotopic analyses. Chloride-free samples were then introduced into an OI Aurora 1030W iTOC interface to the CRDS via an auto-sampler, which purges total inorganic carbon through addition of phosphoric acid followed by wet chemical oxidation of TOC by sodium persulfate. The method was based on Hartland et al. (2012). The $\delta^{13}C_{TOC}$ was measured downstream on a Picarro G2101-i. Measurements were calibrated with potassium hydrogen phthalate (KHP) and compared against isotope ratiomass spectrometer (IRMS) measurements. Raw analytical measurements were corrected to account for the dependence of $\delta^{13}C_{TOC}$ on total C and for the organic carbon contribution from the ion exchange cartridges used to separate Cl^-. These corrections are detailed in Appendix A. Uncertainties in TOC concentration and $\delta^{13}C_{TOC}$ do not exceed 0.05 ppm C and 1.6‰ (2 s.e.) respectively based on replicate analyses of acetate at varied concentrations between 0.5 and 10 ppm TOC.

2.1.3. Experimental blanks

Three blank experiments were performed to ensure that no oxidation or reduction reactions occurred in the absence of the magnetite or in the absence of CO_2. Details of the blank experiment initial conditions are listed in Table 1. Two magnetite- and fluid-free blank experiments were performed in the presence of CO_2 and molecular hydrogen. The measured H_2 concentrations in each experiment remained constant for 4 and 6 days, respectively (Appendix B, Table B.1). A third blank experiment was performed using Ar to purge the headspace over a freshly synthesized magnetite suspension. No organic acids were observed to form in this CO_2-free experiment after 5 days (Appendix B, Table B.1), although this experiment did contain measurable TOC (Table 3).

Table 3. Stable carbon isotope composition of experimental fluids, reagent blanks, and expected end-member C isotope reservoirs. The total organic carbon of experimental fluids is isotopically lighter than the initial supernatant C isotope composition after magnetite synthesis, indicating either mixing between light end-member CO_2 during acetic acid synthesis or partitioning of isotopically heavy organic carbon to the solid phase during experiments. The apparent percent of TOC derived from CO_2 is calculated based on simple mixing of the CO_2 and supernatant blank end-members and is listed in the final column.

Sample	Duration (days)	TOC (ppm)	$\delta^{13}C_{TOC}$(‰)	Apparent% C from CO_2
End-members				

Sample	Duration (days)	TOC (ppm)	$\delta^{13}C_{TOC}$(‰)	Apparent% C from CO_2
CO_2	–	–	−50.69	100.0
Supernatant blank ($n = 2$)	–	3.34	−17.57	0.0
Blanks				
$FeCl_2$ blank	–		−13.25	–
NaOH blank	–	–	−15.35	–
Cartridge blank ($n = 4$)	–	1.01	−24.67	–
Blank 3	5	8.10	−26.89	28.1
High-P experiment				
Exp. 6-2	6	6.61	−26.96	28.3
Exp. 6-3	14	9.66	−29.74	36.7
Exp. 6-4	21	4.12	−18.49	2.78

2.1.4. Reagent blanks

Although no organic acid production was observed in the blank experiments, there was detectable organic carbon in the supernatant fluid from the magnetite synthesis. The form of this carbon is unknown. To account for contaminant carbon present in the reagents, we analyzed the blank TOC and carbon isotope composition of the synthesis reagents, including the CO_2, $FeCl_2$, NaOH, and the initial fluid prior to CO_2 addition. The CO_2 used for the experiments was strongly depleted in ^{13}C ($\delta^{13}C_{VPDB}$ = −50.69 ± 0.05 2 s.e.) compared with the TOC blank on reagents used for magnetite synthesis (Table 3). It was not possible to obtain a reliable measurement of the carbon isotopic composition of the $FeCl_3$ reagent dissolved in doubly deionized (DDI) 18 MΩ water. This reagent could not be passed through the Cl-exchangeable resin due to the formation of precipitate that clogged the resin bed. To account for the contribution of the $FeCl_3$ reagent to the experimental carbon blank, a blank on the TOC of the initial supernatant fluid was obtained. This supernatant blank had $\delta^{13}C_{VPDB}$ = −17.57‰ (Table 3). We assume that the isotopic composition of the supernatant blank is representative of the isotopic composition of contaminant carbon in the experiment to determine the fraction of TOC formed from CO_2.

2.2. Calculations

A series of thermodynamic calculations were performed to evaluate the redox state of the experimental fluids and to determine the thermodynamic potential for acetic acid formation from CO_2. Standard states adopted in this study are unit activity for pure minerals, unit activity of pure H_2O, unit activity of aqueous species in a hypothetical one molal solution referenced to infinite dilution, and unit fugacity of pure gases at 1 bar and 25 °C. The fugacity of both CO_2 and H_2 at the elevated experimental pressures and temperatures were calculated to determine the aqueous hydrogen activity and corresponding thermodynamic affinity of acetic acid formation constrained by metastable equilibrium of reaction 3. Fugacity coefficients of CO_2 and H_2were calculated using a Redlich–Kwong equation of state for quantum and non-polar gas mixtures following Chueh and Prausnitz

(1967) assuming a binary constant k_{ij} of zero, and the supercritical phase mole fraction of CO_2 was calculated following Duan and Sun (2003). Hydrogen activities were calculated from the equilibrium constant for the reaction:

$$H_2(aq) \leftrightarrow H_2(g), \tag{8}$$

where the equilibrium constant is related to the ratio of f_{H_2} to a_{H_2},

$$K = \frac{f_{H_2}}{a_{H_2}}. \tag{9}$$

The log(K) of reaction 8 appropriate to the temperature of interest was obtained from a second-degree polynomial fit to the values of log(K) vs. T at 0, 25, 60, 100, 150, 200, 250, and 300 °C provided in the EQ3/6 thermodynamic database (Johnson et al., 2000). The chemical affinity of reaction 3 for acetic acid formation via CO_2 reduction was calculated as,

$$A = RT\log(K/Q), \tag{10}$$

where K is the equilibrium constant for reaction 3 from Shock (1995), R is the ideal gas constant, T is temperature in Kelvin, and Q is the calculated activity product assuming unit activity of water. The assumption of unit water activity is justified, because in the range of experimental pressures and temperatures, the aqueous activity of water is always >0.96, which amounts to a maximum deviation in log(Q) of less than 5×10^{-2}. Average acetic acid formation rates were calculated with a linear regression of the data, because the increase in acetic acid concentration was linear with time.

2.3. Reaction path modeling

2.3.1. Model description

We used the multicomponent reactive transport code Crunch Flow for reaction path calculations, with no transport specified (Steefel and Lasaga, 1994, Steefel, 2001, Steefel et al., 2014). The primary and secondary species included in all reaction path calculations are listed in Table 4, and the initial conditions of the solid and aqueous phases are listed in Table 4, Table 5 respectively. Thermodynamic data for the aqueous species were compiled from the EQ3/6 database (Johnson et al., 2000), from Shock and Koretsky (1993) for Na-acetate, and from Shock (1995) for the carboxylic acids. Temperature was set to 100 °C in all calculations to facilitate comparison between the different scenarios. Porosity was fixed at 10% in all reaction paths, and the initial primary mineral abundances were chosen such that the Fe(II)-bearing silicate mineral phase was not entirely dissolved. The initial aqueous primary O_2 concentration was assigned a value in equilibrium with the relevant mineral buffer assemblage (i.e., DKQM or QFM), and the initial aqueous HCO_3^- was equilibrated with an initial acetic acid concentration of $\sim 10^{-7}$ M (Table 5). Reaction path results are cast in terms of a_{H_2} and the activity of aqueous total organic carbon (a_{TOC}), where the secondary aqueous H_2 is assumed to be in equilibrium with the primary aqueous O_2 species. We define the aqueous TOC activity (a_{TOC}) as the sum of the activities of all aqueous OC species multiplied by their respective carbon numbers to quantify the total amount of CO_2 reduced to organic species. Reaction path calculations were run with no flow into or out of the domain to model closed-system behavior. The mineral and aqueous

reactions controlling the evolution of the solid and aqueous reaction path constituents are detailed in Sections [2.3.2 Aqueous reactions](#), [2.3.3 Mineral dissolution and precipitation reactions](#)below.

Table 4. Aqueous species, gases and mineral phases used in Crunch Flow reaction path calculations.

Primary species	Secondary species	Secondary Species Cont'd.
H^+	CH_3COO^- (acetate)	$HCOO^-$ (formate)
$O_2(aq)$	$CO_2(aq)$	CH_3COO^- (acetate)
HCO_3^-	CO_3^{2-}	C_2H_5COOH (propanoic acid)
Na^+	$Na(CH_3COO)^{2-}$	$C_2H_5COO^-$ (propanoate)
Cl^-	$NaCH_3COO(aq)$	C_3H_7COOH (butanoic acid)
CH_3COOH (acetic acid)	$NaCO_3^-$	$C_3H_7COO^-$ (butanoate)
$SiO_2(aq)$	$NaCl(aq)$	C_4H_9COOH (pentanoic acid)
Al^{3+}	$NaHCO_3(aq)$	$C_4H_9COO^-$ (pentanoate)
Fe^{2+}	$NaOH(aq)$	$C_5H_{11}COOH$ (hexanoic acid)
Gases	OH^-	$C_5H_{11}COO^-$ (hexanoate)
O_2	Fe^{3+}	$C_6H_{13}COOH$ (heptanoic acid)
H_2	$CO(aq)$	$C_6H_{13}COO^-$ (heptanoate)
CO_2	$H_2(aq)$	$C_7H_{15}COOH$ (octanoic acid)
CO	$HCOOH$ (formic acid)	$C_7H_{15}COO^-$ (octanoate)

Minerals	Initial volume fraction	Surface area (m^2/g)	Rate at 25 °C ($mol\ m^{-2}\ s^{-1}$)	E_a($kJ\ mol^{-1}$)
QFM(S) assemblage				
Quartz	0.964	1.0	1.2589×10^{-14}	87.50
Fayalite	0.035	10	1.00×10^{-13}	62.76
Magnetite	0.001	1.0	1.66×10^{-11}	18.60
Siderite[a]	0.0	1.0	0.60×10^{-9}	41.87
DKQM(S) assemblage				
Daphnite	0.034	100	1.00×10^{-14}	58.62
Kaolinite	0.0	1.0	1.00×10^{-13}	62.76
Quartz	0.965	1.0	1.2589×10^{-14}	87.50
Magnetite	0.001	1.0	1.66×10^{-11}	18.60
Siderite[a]	0.0	1.0	0.60×10^{-9}	41.87

[a] Siderite was only allowed to form in two of the four reaction path scenarios. Only reaction paths without siderite are shown in [Fig. 5](#).

Table 5. Initial aqueous [fluid compositions](#) of the primary species used for the reaction path calculations. The IC and OC species are equilibrated with respect to reaction 11 and with respect to the mineral assemblage at a total initial PCO_2 of 10^{-2} bars for DKQM(S) and 10^{-6} for QFM(S) at 100 bars total pressure and 100 °C.

Primary Species	QFM(S)	DKQM(S)
log(Total Ac)[a] (M)	−6.7	−6.9
log(O_2(aq)) (M)	−64.2	−60.4
log(HCO_3^-(aq)) (M)	−6.8	−3.9
H^+	Charge	Charge
Na^+ (M)	0.8	0.8
Cl^- (M)	0.8	0.8
SiO_2(aq)	Quartz	Quartz
Fe^{2+}	Magnetite	Magnetite
Al^{3+}	–	Kaolinite

[a] "Total Ac" represents "total acetic acid," or the total concentration of secondary reduced carbon species cast in terms of the molar mass of acetic acid, which was used as a basis species in all reaction path calculations.

Carbon dioxide injection was simulated by specifying a constant flux of CO_2 into the system starting from an initial equilibrated acetic acid concentration with PCO_2=0.01bars at a constant total pressure of 100 bars. This was accomplished by creating a hypothetical phase that dissolved to release CO_2(g) irreversibly and at a constant rate, where the release rate of CO_2 was proportional to the assigned rate constant. To make direct comparisons between reaction path scenarios, 100 bars of CO_2 (in the absence of reduction) was injected into the system in every calculation. The CO_2 release rate was specified in all reaction path input files to be fast relative to the rates of both mineral dissolution and acetic acid formation, simulating rapid CO_2 injection during GCS.

2.3.2. Aqueous reactions

The reaction path modeling approach assumes homogeneous equilibrium among all aqueous primary and secondary species listed in Table 4, except for acetic acid, which is allowed to form from IC according to:

$$2H^+ (aq) + 4H_2 (aq) + 2HCO_3^- (aq) \leftrightarrow CH_3COOH(aq) + 4H_2O. \qquad (11)$$

The rate of this reaction was determined from the results of the hydrothermal experiment conducted at ~100 °C. Speciation of the OC was completed using acetic acid as a primary species in equilibrium with a suite of secondary OC species hypothesized to obtain metastable equilibrium with IC in petroleum reservoirs (Helgeson et al., 1993; Table 4). Organic species that are very slow to equilibrate (e.g., CH_4) were excluded from the secondary species considered in these models.

2.3.3. Mineral dissolution and precipitation reactions

Given the mineralogic complexity of reservoirs considered for GCS, we consider two simplified model end-member mineral reactions in our analysis of the reservoir redox environment and the reduction of CO_2:

(1) quartz–fayalite–magnetite (QFM) ± siderite (QFMS), and

(2) chlorite/smectite Fe(II) end-member daphnite–kaolinite–quartz–magnetite (DKQM) ± siderite (DKQMS).

These end-members were chosen as hypothetical reaction buffers to model the apparent redox extremes of sedimentary reservoirs (Fig. 1). The supply of Fe(II) to the aqueous phase limits the rate of CO_2 reduction, so the trapping of CO_2 by reduction is sensitive to the surface reaction kinetics of the primary Fe(II)-bearing silicate minerals. To approximate the time scales for mineral dissolution and secondary mineral precipitation, we use the rate constants and activation energies reported in Xu et al. (2004) for primary and secondary silicate and carbonate minerals (Table 4). The corresponding rate constant and activation energy for the formation of secondary magnetite were not provided in Xu et al. (2004), so we assumed the values reported by White et al. (1994) for magnetite dissolution (Table 4). This assumption does not impact the final outcome of the simulations, because the evolution of the system is controlled primarily by the dissolution kinetics of the Fe(II)-bearing silicate phase. The specific surface area (SSA) of daphnite was set to 100 m^2/g, and the SSA of fayalite was assumed to be a factor of 10 less.
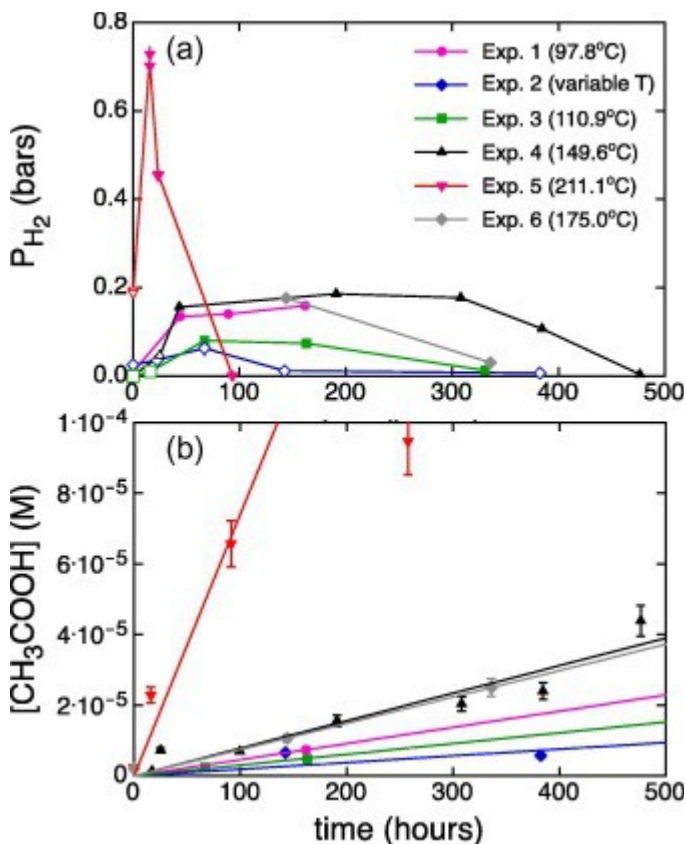
3. Results

3.1. Experimental CO_2 reduction by magnetite

A total of six hydrothermal experiments were performed to investigate the reactivity of CO_2 under GCS-analog conditions. Experiment durations ranged from several days to weeks with continuous rocking of the hydrothermal apparatus. Aqueous fluid and supercritical-CO_2 (sc-CO_2) phases were routinely sampled to monitor the hydrogen fugacity of the system and to track the formation of organic species (Table 2). The three most significant changes observed in every experiment were (1) the initial increase of PH_2 up to 715 mbar, (2) the subsequent decrease of PH_2, and (3) the synthesis of acetic acid up to 9.6×10^{-5} M (Table 2). Measured H_2 concentrations were used to determine metastable equilibrium among carbon species, and time-resolved measurements of organic acid concentrations were used to explore the kinetics of abiotic CO_2 reduction by magnetite.

3.1.1. Production and loss of hydrogen

The PH_2 of gases sampled from the sc-CO_2 phase evolved throughout the course of each experiment. Results are summarized in Table 2 and graphically illustrated in Fig. 2a. With the exception of Exp. 5, the PH2 initially increased, followed by an extended period of reasonably constant PH2 that varied in duration among the different experiments. The observed increase in PH_2 was due in part to the heating of the reactor with a fixed supercritical fluid phase volume, leading to a pressurization of the H_2 injected during the experimental setup. In some cases, the mole fraction of H_2 in the supercritical phase also increased substantially, indicating H_2 production (i.e., Exp. 1, 3 and 4). The magnitude of increase in H_2 mole fraction cannot be explained by changing CO_2 or H_2 solubility with pressurization and heating. We interpret H_2 production to be the result of aqueous Fe(II) oxidation and subsequent precipitation of magnetite. Following the synthesis procedure, the composition of the aqueous phase was controlled by equilibrium between magnetite and the NaCl-rich fluid. The initial aqueous Fe(II)

concentration was calculated using Crunch Flow, assuming fluid equilibrium with magnetite at the glovebox $P\text{H}_2$ of 0.05 and the ambient laboratory temperature of 22 °C. According to these calculations, up to 50 mM Fe(II) was in the fluid phase in the H_2-enriched glovebox environment. Chemical speciation calculations indicate that with increasing temperature, this Fe(II)-rich aqueous solutionbecomes supersaturated with respect to magnetite leading to H_2 production (i.e., reaction 7). The concentration of aqueous Fe is highly sensitive to both redox environment and pH, so it is possible that the variability in hydrogen production between experiments was caused by differences in time spent on the experimental setup, during which the suspension was exposed to air.
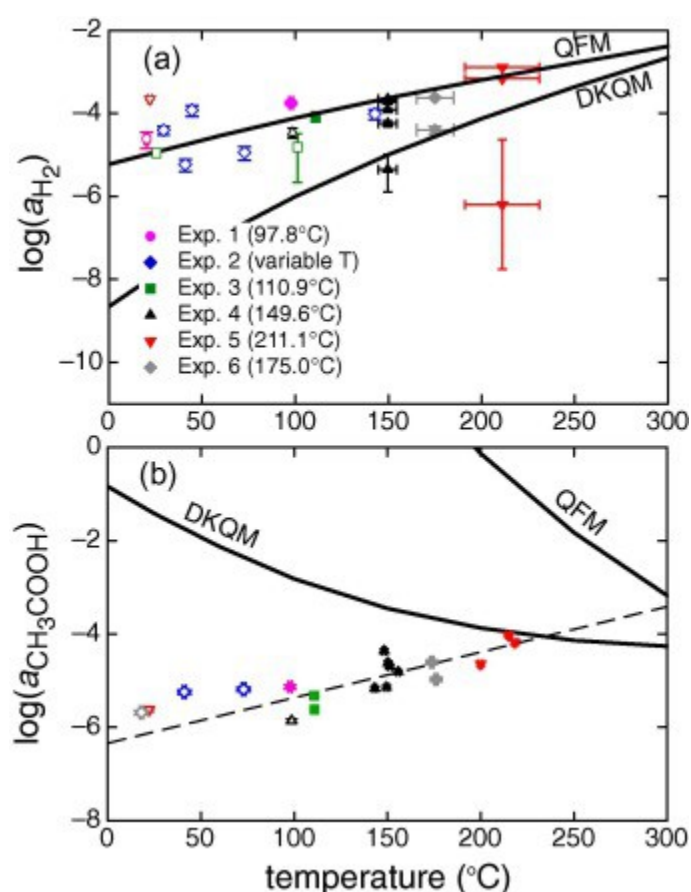

[Download high-res image (283KB)](#)

[Download full-size image](#)

Fig. 2. Analytical results of reaction cell experiments including (a) hydrogen partial pressures calculated from measured sc-CO2 phase hydrogen concentrations and total pressures, where hydrogen pressures based on concentrations measured before a steady state temperature was obtained are drawn as open symbols, and (b) measured acetic acid concentrations as a function of time. Open symbols in (a) denote samples obtained prior to or in the absence of temperature stabilization in the reaction cell. The fastest rate of acetic acid formation occurred at the highest temperatures (i.e., experiment 5 > 200 °C). Lines in (b) are linear regressions of the acetic acid vs. time data. The final data point from Exp. 5 was excluded from the regression, because hydrogen concentrations were negligible at the time of sample collection.

Activities of H_2(aq) computed from the analytical data in Table 2 are plotted as a function of experimental temperature in Fig. 3a, where it can be seen that hydrogen activities largely cluster near QFM at temperatures <100 °C, and largely between QFM and DKQM at higher temperatures. Only

two measured values are more oxidizing than required by DKQM equilibrium ([Fig. 3](#)a). Measured H_2 [partial pressures](#) eventually decreased to very low values in most experiments indicating gradual oxidation of our experimental system ([Fig. 2](#)a). The observed oxidation may be due the consumption of H_2 during CO_2 reduction or due to the loss of H_2 during sampling. Although we cannot determine the primary cause of the H_2 loss with certainty, a fraction of the H_2 may have been consumed by CO_2 reduction, for example, reaction 3; however, measured acetic acid concentrations can only account for a small fraction (up to about 10%) of the H_2 loss on a per mole basis. Complete oxidation of magnetite to Fe(III)-oxide/hydroxide was only observed in Exp. 2, which was allowed to run for an extended period time following the drawdown of hydrogen. In this case, the final experimentally produced mineral phases were identified using XRD to be a mixture of [goethite](#) and [hematite](#)([Supplementary Materials, Fig. S.2](#)).

[Download high-res image (266KB)](#)

[Download full-size image](#)

Fig. 3. (a) Equilibrium hydrogen activity of the reaction cell experiments as a function of temperature during initial heating of the reaction cell (open symbols) and under approximately constant temperature conditions (closed symbols). Experimental data obtained at low temperatures prior to reaching a constant temperature or when temperatures were variable are shown as open symbols. The a_{H_2} of most experimental fluids remained within the QFM–DKQM buffer range. (b) Measured [acetic acid](#) activities for all experiments compared with QFM and DKQM buffer equilibrium values calculated assuming 100 bars total CO2 pressure and unit activity of aqueous H2, CO2, and acetic acid. Acetic acid formation from CO2 was thermodynamically favorable at all times during the experiments. The dashed line in (b)

illustrates the approximate temperature at which acetic acid could equilibrate with CO2 in experiments with a_{H_2} consistent with QFM buffering on timescales of days to weeks, around 300 °C.

3.1.2. Organic acid synthesis

Formation of organic acids was observed in every experiment containing CO_2 (Fig. 2b), while no organic acids were observed to form during a blank experiment containing the magnetite suspension with an inert Ar headspace (Appendix B, Table B.1). The production of organic acids has been previously detected in the presence of CO_2 and magnetite across a range of temperatures representative of hydrothermal systems (125–350 °C; Chen and Bahnemann, 2000, McCollom and Seewald, 2003a). Here, we observe organic acid formation at slightly lower temperatures (~100 °C) compared to previous studies. The dominant species formed was acetic acid (1.4×10^{-6}–9.5×10^{-5} M), with minor formic acid (below detection to 7.9×10^{-5} M) and glycolic acid (below detection to 2.3×10^{-5} M). Formic and glycolic acid were not consistently observed in all experiments. Measured acetic acid concentrations are listed in Table 2. These analyses did not include measurements of alkanes or other hydrocarbons, so we cannot rule them out as potential products.
The carbon isotopic composition of total organic carbon was measured periodically during Exp. 6 to determine the relative proportion of TOC formed from the CO_2 initially injected into each experiment (Table 3). High concentrations of organic acids in petroleum reservoirs are commonly attributed to thermal degradation reactions, where complex organic molecules are broken down into shorter chain organic molecules, including methane and carboxylic acids (Carothers and Karaka, 1978, Bell et al., 1994, Knauss et al., 1997). Given the possibility of generating organic acids from organic matter, it is necessary to trace the source of carbon incorporated into the dissolved OC using C isotopes. We calculated the fraction of synthesized OC formed from the ^{13}C-depleted CO_2 assuming the blank organic $\delta^{13}C_{VPDB}$ composition was identical to the supernatant blank of −17.57‰ (Table 3). After 1 and 2 weeks of the experiment respectively, we calculate that 29% and 37% of the OC was derived from the CO_2 (Table 3).
Only three samples from Exp. 6 were taken, because large volumes of fluid (>9 mL) were required to make these isotopic analyses, and the total volume of the reaction cell is limited. We infer that the isotopic results from the other experiments (i.e., Exp. 1 through 5) would be similar, but no samples of sufficient size were collected from these experiments for determination of $\delta^{13}C_{VPDB}$. In addition, these analyses are not compound-specific, so the amount of acetic acid formed directly from the ^{13}C-depleted CO_2 was not directly quantified. It is possible that the measured organic acids formed entirely from CO_2 reduction but that their contribution to the total isotopic signature is obscured by the initial blank OC. Collectively, these experimental results demonstrate that CO_2 is incorporated into OC species, and that acetic acid can be formed from inorganic carbon in the presence of a mineral such as magnetite.

4. Discussion

The results of hydrothermal experiments indicate that reactions among IC and OC species are kinetically accessible in systems with pressure, temperature, and PCO$_2$ values typical of GCS. In the

following section, we evaluate the thermodynamic driving force for acetic acid formation under GCS conditions, and we use our experimental results to determine the rate constant and activation energy of acetic acid formation. We then apply these kinetic results in a series of reaction path scenarios to evaluate the impact of CO_2 reduction on mineral stability and on the long-term fate of CO_2 during GCS.

4.1. Thermodynamic and kinetic constraints on H_2 and organic acid dynamics

To understand the driving force for both hydrogen and acetic acid production, we performed a series of thermodynamic calculations based on the measured experimental aqueous and supercritical phase compositions. Aqueous H_2 concentrations were strongly controlled by temperature, while acetic acid concentrations had a linear dependence on time.

4.1.1. Thermodynamic evaluation of experimental results

The chemical affinity of reaction 3 for acetic acid production under our experimental conditions are reported in Table 2 to indicate the thermodynamic potential for CO_2 reduction to acetic acid. Calculated reaction affinities are significantly greater than required for equilibrium, with most values between ∼500 and 1000 kcal/mol at temperatures >170 °C, indicating the strong thermodynamic potential for acetic acid formation from IC. The expected activity of acetic acid at equilibrium at equilibrium with the QFM and DKQM buffer assemblages was estimated according to Eq. (4), and measured acetic acid concentrations were less than the calculated buffer values as illustrated in Fig. 3b. The acetic acid concentration was only observed to decrease after an initial increase in Exp. 2, but the magnitude of the decrease is within experimental uncertainty. There was also a time lag between the onset of decreasing PH_2 and the onset of decreasing acetic acid production rate in the experiments. Acetic acid concentrations were never observed to decrease prior to H_2 loss.

### 4.1.2. Kinetics of organic acid synthesis

The experimental results presented above suggest that organic acids, primarily acetic acid, formed from CO_2 and H_2 when a reactive mineral (magnetite) was present. To investigate the kinetics of CO_2 reduction in the presence of magnetite, and to further assess the extent to which magnetite catalyzed the conversion of CO_2, experiments were performed at several different temperatures from 100–215 °C. As illustrated in Fig. 2b, the measured acetic acid concentration is a linear function of the duration of the experiment, suggesting zeroth-order reaction kinetics independent of the calculated chemical affinity and reactive surface area. Zeroth-order reaction kinetics may arise if the reactant binds strongly to the promoting mineral surface. Although it is not possible for us to rule out several different pathways for the formation of acetic acid in these experiments, the zeroth-order rate dependence is similar to the kinetic behavior of acetic acid decomposition via thermal decarboxylation in the presence of magnetite (Palmer and Drummond, 1986) and to the dehydrogenation of gas-phaseformic acid on magnetite (Mars et al., 1963). Other studies observed first-order decarboxylation and oxidation kinetics of acetic acid, acetate, formic acid, and formate in the presence of magnetite (McCollom and Seewald, 2003a, McCollom and Seewald, 2003b).

The acetic acid concentrations depicted in Fig. 2b were used to calculate the rate of acetic acid formation as a function of temperature (Table 6). Acetic acid formation accelerated with increasing T (Fig. 2b). Faster acetic acid formation was also associated with a relatively rapid decline in PH2 (Fig. 2a). Although we do not fully understand the processes controlling H_2consumption in these experiments, the increase in the rate of H_2consumption with increasing temperature suggests that this process was thermally activated. The eventual oxidation of the experimental systems could be associated with the reduction of CO_2, although H_2 removal during sampling could also account for the observed changes.

Table 6. Acetic acid formation rates observed in the GCS-analog reaction cell experiments. Acetic acid is abbreviated as "Ac".

Experiment	Average T(°C)	Rate (μmol Ac L^{-1} day^{-1})	Rate error (2 s.e.) (μmol Ac L^{-1} day^{-1})	$1000/T$(K^{-1})
Exp. 1	97.8	1.10	0.22	2.69
Exp. 2	Variable	0.43	0.07	Variable
Exp. 3	110.9	0.77	0.11	2.60
Exp. 4	149.6	1.81	0.14	2.37
Exp. 5	211.1	20.7	3.09	2.07
Exp. 6	175.0	1.78	0.25	2.23

The temperature dependence of acetic acid formation kinetics is consistent with an Arrhenius-type rate dependence. Assuming a quasi zeroth-order reaction rate term, the rate coefficient (k) is equivalent to the slope of acetic acid concentration as a function of time. The apparent activation energy (E_a) was calculated from the slope of log(k) vs. the inverse of average experimental temperature (Fig. 4). Error in the calculated E_a was determined by linear regression of the data using ±10 °C uncertainty in temperature and the 2 standard deviation (s.d.) error in k calculated for each experiment (Table 6). The calculated E_a for acetic acid formation is 47 ± 16 kJ/mol (2 s.d.), which is greater than the activation energy for acetic acid formation during hydrous pyrolysis of oil shale (22.72 kJ/mol; Barth et al., 1989).
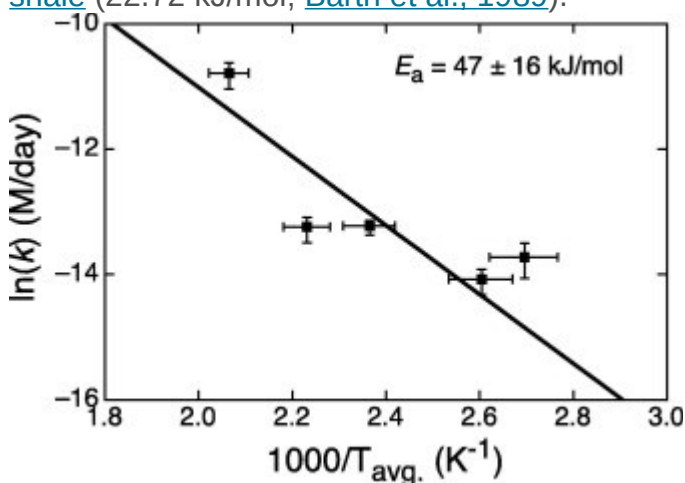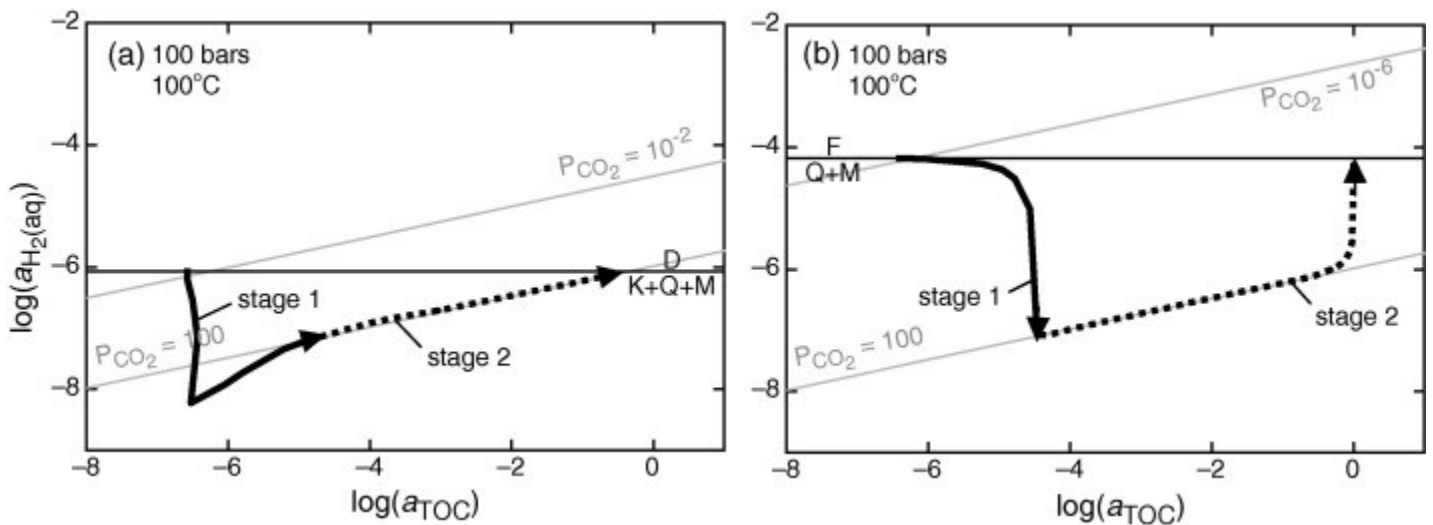

Download high-res image (99KB)

Fig. 4. Arrhenius-type plot of zeroth-order rate coefficients for [acetic acid](#) formation. The acetic acid formation rates are linear with respect to inverse temperature. The slope of these data is consistent with an [activation energy](#) for acetic acid formation of ~47 kJ/mol. This activation energy barrier is about a factor of 2 greater than previously published activation energies for acetic acid formation through hydrous pyrolysis in [shale](#). Temperatures fluctuated significantly in Exp. 2, so the acetic acid formation rate from this experiment is not included in the analysis.

4.1.3. Theoretical analysis of the effect of CO_2 on reservoir redox environments

We present a series of hypothetical reaction path calculations to explore the impacts of CO_2 reduction on the stability of reservoir mineral constituents and the reactivity of CO_2 during GCS. These calculations are based on the assumption that carbon can undergo redox reactions in certain reservoirs on timescales comparable to the rates determined experimentally here. The measured activation energy of acetic acid formation from CO_2 in the presence of magnetite is sufficiently low to allow for measurable conversion, even at the temperatures typical of sedimentary reservoirs proposed for GCS. The acetic acid formation rate used in these calculations was 0.77 M day^{-1} from Exp. 3, which was conducted at an average temperature of 110.9 °C ([Table 6](#)). In these reaction path calculations, we assume that the solid phase consists of two Fe(II)-bearing mineral assemblages, QFM and DKQM. These are hypothetical assemblages that were chosen because they bracket the range of a_{H_2} inferred for real [sedimentary basins](#) (i.e., [Fig. 1](#)). Two additional calculations were performed in which [siderite](#) was allowed to form. The redox activity of [sulfur](#) and complex organic compounds such as [kerogen](#) are not discussed here, but are likely to play a role in [redox conditions](#) within [petroleum reservoirs](#).

The effects of introducing the same amount of CO_2 into reservoirs buffered by DKQM and QFM are illustrated in [Fig. 5](#)a and b, respectively. Over the course of both reaction paths, the injection of CO_2 leads to extensive conversion of CO_2 to OC. In the hypothetical QFM and DKQM reservoir buffering scenarios, 2026 and 1032 moles of CO_2 are reduced per cubic meter of [fayalite](#) and daphnite reacted, respectively. This equates to more than 0.04 moles of CO_2 reduced to OC per mole of Fe(II) in the primary [silicate](#) phase. These trapping rates are on par with the [carbon sequestration](#) potential attributed to mineral carbonation in saline [aquifers](#) (cf. Xu et al., 2012).

Fig. 5. Reaction path calculations depicting the evolution of total organic carbon and hydrogen activities in reservoirs initially containing the Fe(II)-silicate minerals (a) daphnite and (b) fayalite. Arrows are used to delineate the two primary stages of both reaction paths. Stage 1 includes the initial CO2 injection and equilibration among IC and OC species, and stage 2 includes the eventual equilibration of IC and OC with the solid mineral assemblage. The same amount of CO2 was pumped into the system in both of these reaction paths. The equilibration of IC and OC resulting from CO2injection during stage 1 occurs within 103 years, resulting in an a_{H_2} that is no longer equilibrated with the initial mineral assemblage. Equilibrium with respect to the existing mineral assemblage is obtained within 106 years, during which time secondary minerals are formed and some or most of the injected CO2 is reduced to organic carbon species.

Redox conditions in both reaction paths evolve in two distinct stages. Stage (1) is characterized by a rapid oxidation of the system upon initial injection of CO_2, where a_{H_2} continues to decrease until IC and OC are equilibrated at $PCO_2=100bars$. The duration of this stage is approximately 10^3 years and is controlled by the kinetics of acetic acid formation. In stage (2), the slow dissolution of the Fe(II)-silicate mineral supplies an electron donor that drives the reduction of injected CO_2 to organic carbon. This phase occurs over much longer timescales, around 10^6 years, during which the primary Fe(II)-silicate mineral is oxidized and converted into secondary kaolinite, quartz, and magnetite (DKQM) or secondary quartz and magnetite (QFM). The extent of CO_2 reduction is greater in the case of the QFM-buffered reaction path, because fayalite in equilibrium with magnetite buffers a_{H_2} at a higher value, increasing the chemical potential for the reduction of CO_2. Based on the stoichiometry of reactions 3, 5, and 6, the production of acetic acid requires the oxidation of Fe(II) and the consumption of CO_2 at a ratio of 4:1. Thus, reduction of CO_2 to organic acids in GCS reservoir may be limited by the availability and kinetics of Fe(II)-silicate mineral oxidation in the reservoir, unless other reactions are regulating the a_{H_2}.

The results of these reaction path calculations can be clarified by considering the two main reactions: reaction 3 consumes H_2 while reducing CO_2 to acetic acid and reaction 7 produces H_2 by oxidizing Fe(II) to form magnetite. In stage (2), H_2 consumption by CO_2 proceeds more quickly than H_2 production during Fe(II)-silicate oxidation (Fig. 5a and b). The reduction of CO_2 ceases when IC

and OC are equilibrated with the mineral assemblage. Equilibrium among IC and OC species and among solid mineral phases is not mutually exclusive but occurs on very different timescales. Thus, the eventual re-equilibration of silicate minerals with a_{H_2} will likely be limited by the slow kinetics of primary mineral dissolution in GCS reservoirs.

In the reaction path scenarios discussed above, consumption of CO_2 was limited to the formation of organic molecules. However, siderite precipitation is also thermodynamically favorable directly following CO_2 injection into both assemblages and is likely an alternate reaction pathway in competition with CO_2 reduction. The oxidation of Fe(II) to Fe(III) is coupled to the reduction of CO_2 to organic molecules, so siderite precipitation will reduce the availability of Fe(II) and limit organic molecule formation. In a final set of reaction path calculations, siderite was allowed to form in both mineral-buffered assemblages (i.e., DKQMS and QFMS). Siderite precipitation initially decreases both the a_{H_2} and TOC content of both systems. However, equilibration among the solid phases causes the eventual conversion of a fraction of the precipitated siderite to magnetite, leading to CO_2 reduction and an eventual return to the initial a_{H_2}. Addition of siderite to the DKQM reaction path significantly reduces the final total organic carbon concentration from log(TOC) = −0.81 to log(TOC) = −5.52. In the QFM reaction path calculation with siderite, all of the siderite is eventually converted to magnetite, yielding an identical final TOC once the IC and OC species have equilibrated with the mineral assemblage. Thus, we conclude that siderite formation will not reduce the long-timescale extent of CO_2 trapping by reduction in fayalite-rich (e.g., basaltic and ultramafic) GCS reservoirs but may provide a barrier to CO_2 reduction in sequestration reservoirs containing more oxidized primary mineral assemblages.

Natural sedimentary reservoirs are inherently complex multi-component systems for which innumerable reaction pathways can be constructed depending on the suite of reactions that are allowed to occur over timescales and under the conditions considered reasonable by the modeler. In the absence of any *a priori* knowledge of reaction kinetics for all of the possible phases that can form along a given metastable reaction path, it is necessary to seek constraints from natural geologic reservoirs. Acetic acid and higher carbon number organic acids are ubiquitous in relatively low-*T*, organic-rich oil and gas formations, and as discussed above, the relative concentrations of these species are consistent with metastable equilibrium among IC and OC in geologic reservoirs. As such, we consider the formation of these species to be both reasonable and likely outcomes of CO_2 injection into sedimentary basins in which CO_2 reduction is thermodynamically favorable. The trapping of CO_2 by reduction in natural geologic reservoirs, which are intrinsically open systems, will likely be favored at higher temperatures where both primary mineral dissolution and CO_2 reduction kinetics are accelerated.

Mineralogic transformations predicted to occur as a result of reservoir oxidation by CO_2 have been observed at the Ladbroke–Katnook Reservoir, which is a natural analog for CO_2 sequestration in chlorite-bearing geologic reservoirs (Watson et al., 2004). In this system, reservoir rocks were exposed to magmatic CO_2 in some places and remained pristine in others, facilitating an analysis of

the effects of CO_2 exposure over geologic timescales. The relatively large fraction of chloritic minerals contained in the pristine reservoir rock (~5% to 7%) was significantly diminished (<2%) in the rocks exposed to CO_2 and replaced by Mg- and Fe-carbonates, clays, and quartz. This suite of transformations is qualitatively consistent with crossing from chlorite(represented in our model by the end-member daphnite) stability into the quartz–kaolinite–magnetite–siderite stability field (see Fig. 1), although no Fe-oxide mineral phases were detected during characterization by XRD (Watson et al., 2004). Such transformations would be expected if CO_2 addition led to reservoir oxidation, prior to the re-equilibration of the solid mineral assemblage. Aqueous organic acid concentrations were not reported in this study, so it is not possible to evaluate the chemical affinity of acetic acid formation in the reservoir. In future, measurement of aqueous organic acid concentrations and isotopic compositions in similar GCS-analog systems would provide further constraints on the likelihood and extent of CO_2 trapping by reduction.

4.2. Enhancing trapping with CO_2 reduction

The goal of GCS is the long-term storage of CO_2 in the subsurface. In the short term, appropriate reservoir engineering strategies must be implemented to optimize the volume of CO_2 stored in a given reservoir as well as the mitigation of volumetric leakage along preexisting well bores and fractures. In contrast, the long-term fate of CO_2 in the subsurface will be dictated by the chemical reactivity of the CO_2 phase with the reservoir minerals. Selection of target reservoirs must be performed with a view to enhancing the long-term stability of the storage site.
According to the results of our experiments, the abiotic reduction of CO_2 to acetic acid on the surfaces of nanoparticulate magnetite is kinetically accessible and thermodynamically favorable under GCS conditions. Assuming an equilibrium acetic acid concentration of approximately $10^{-3.8}$ M for a DKQM-buffered reservoir (Fig. 3b) and an acetic acid formation rate of ~20 µM day^{-1} (Table 6), the equilibration of acetic acid with CO_2 can occur within a month at around 200 °C. This formation rate may not be directly transferrable to acetic acid formation in natural reservoirs, because the surface properties and reactivity of natural magnetite may differ from those of the freshly synthesized magnetite used in these experiments. However, experimental studies in which CO_2 was reacted with the chamosite-rich Ladbroke Grove sandstone resulted in the precipitation of a nanoparticulate Fe-oxide thought to be magnetite (Luquot et al., 2012), similar to the material used to catalyze CO_2 reduction here. Reduction of CO_2 to acetic acid can also be promoted by other biologically-mediated processes (Ohtomo et al., 2013). In general, laboratory-derived reaction rates can differ from field-derived rates by orders of magnitude (cf. Appelo and Postma, 2005, Mohd Amin et al., 2014), so additional kinetic constraints for the formation of acetic acid and other kinetically accessible organic species (cf. Table 4) should be sought from GCS-analog and pilot reservoirs.
Both carbon reduction and reservoir mineral oxidation will likely enhance the long-term stability of stored CO_2. Extensive dissolution and precipitation reactions can lead to volumetric increases in the mineral phases, which will occlude pore spaces and decrease overall reservoir permeability. In addition, the reduced carbon species that are formed from CO_2 will be less prone to volumetric

leakage, because they are either more soluble or have a higher [interfacial tension](#) with the aqueous phase. A significant increase in the concentration of organic acids resulting from CO_2 reduction could also enhance ligand-promoted dissolution of the primary silicate minerals (e.g., [Stillings et al., 1996](#), [Drever and Stillings, 1997](#), [Ganor et al., 2009](#), [Shao et al., 2011](#), [Lawrence et al., 2014](#); etc.), which could in turn accelerate both carbonate mineralization and carbon reduction through mobilization of redox active-metals. [Sorption](#) of organic acids at mineral surfaces provides an additional stabilization mechanism for the injected carbon ([Johnson et al., 2004](#), [Ganor et al., 2009](#), [Lawrence et al., 2014](#)). Storage of CO_2 in [ultramafic rocks](#) that contain abundant Fe(II) silicates and [oxides](#) has also been discussed as a strategy for enhancing carbonate mineralization ([Kelemen and Hirth, 2012](#)), but systems rich in fayalite will also favor CO_2 trapping by reduction. Volumetric increases in mineral phases associated with the conversion of primary silicates to [secondary minerals](#) during carbon reduction in these formations may further promote the fracturing of the massive ultramafic rock (e.g., [Kelemen and Matter, 2008](#)), enhancing CO_2 permeability. Thus, reservoirs containing mineral assemblages expected to undergo major post-injection shifts in f_{H_2} (i.e., those containing Fe(II)-silicates and [sulfide](#) minerals) could be considered favorable candidates for GCS.

5. Conclusion

The reduction of CO_2 is thermodynamically favorable in geologic reservoirs containing reducing mineral assemblages that are currently being considered for GCS. The surfaces of Fe(II)-oxide and -silicate minerals are known to facilitate redox reactions involving both carbon and other contaminant species. In this study, we demonstrated that [magnetite](#) suspended in an Fe(II)-bearing NaCl brine can promote the abiotic reduction of CO_2 to [acetic acid](#). The [activation energy](#) for acetic acid formation determined experimentally is consistent with field observations of metastable equilibrium between IC and OC that require IC reduction to be kinetically accessible.

The stable long-term storage of CO_2 during GCS can be enhanced by selecting reservoirs containing abundant Fe(II)-silicate minerals. Based on reaction path calculations completed using the measured acetic acid formation kinetics, CO_2 reduction to organic species could provide a trapping capacity similar in magnitude to that of mineral carbonation. The redox activity of CO_2 in the subsurface is a potentially important component of GCS reservoir geochemistry that could significantly affect the evolution and long-term fate of CO_2 storage reservoirs.

Acknowledgements

Appendix. A. Corrections to raw CRDS data

Data processing was performed to correct raw CRDS $\delta^{13}C$ values (1) for a concentration bias at aqueous carbon concentrations less than 5.0 ppm, and (2) for the carbon derived from carbon on the Dionex OnGuard Ag ion exchange cartridges used to remove chloride. The first correction was

completed by fitting a fourth-order polynomial curve to measured $\delta^{13}C$ (‰) as a function of carbon concentration (Fig. A.1). Fitted parameters are listed in Table A.1. This correction was applied to all samples with measured carbon concentrations less than 5.0 ppm, because the polynomial fit only applies to these concentrations. The second correction was applied by assuming mixing between cartridge-derived carbon with an isotopic composition of $\delta^{13}C = -24.667$‰ (Table 3) and a concentration of 1.01 ppm in the cartridge effluent. A constant concentration of cartridge-derived carbon was assumed, because the same volume of sample was passed through the same number of cartridges for every analysis where cartridges were used.
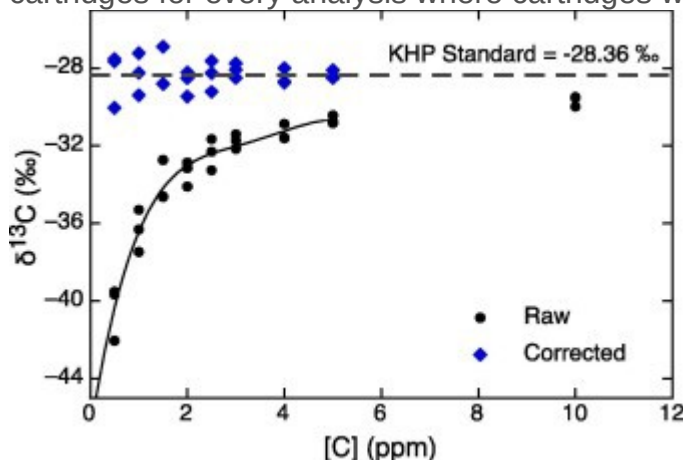
Download high-res image (104KB)

Download full-size image

Fig. A.1. Raw measurements of δ13C (‰) for the KHP carbon isotopic standard depend on carbon concentration, especially when [C] < 5.0 ppm. Reported concentrations are corrected based on the fourth-order polynomial fit to the raw data depicted as a black line. Fitted parameters are listed in Table A.1. Corrected δ13C values are consistent with the average isotopic composition of the KHP standard (−28.36‰).

Table A.1. Fitted polynomial correction parameters. Raw sample values (x) with measured carbon concentrations less than 5.0 ppm were corrected (y) using the following expression: $y = x + Std - (Ax^4 + Bx^3 + Cx^2 + Dx + E)$.

Parameter	Value
A	−0.094
B	1.311
C	−6.730
D	15.843
E	−46.755
Std	−28.36

Appendix. B.

Table B.1. Results of experimental blanks monitoring PH2 and the formation of acetic acid ("Ac").

Sample	Time (h)	T (°C)	P (bars)	[H$_2$] (ppm)	PH2 (bar)	Log[Ac] (M)
Blank 1-1	72	108	410	577	0.24	n.a.

Sample	Time (h)	T (°C)	P (bars)	[H$_2$] (ppm)	PH2 (bar)	Log[Ac] (M)
Blank 1-2	120	103.3	384	507	0.19	n.a.
Blank 1-3	144	103.3	378	732	0.28	n.a.
Blank 2-1	0	20	57	1015	0.06	n.a.
Blank 2-2	24	93.9	91	1034	0.09	n.a.
Blank 2-3	96	93.2	88	1059	0.09	n.a.
Blank 3-1	0	20	1	n.a.	n.a.	−5.82
Blank 3-2	24	115.7	n.a.	n.a.	n.a.	b.d.
Blank 3-3	120	133.7	1	n.a.	n.a.	b.d.

n.a. = not analyzed.

b.d. = below detection.

Appendix C. Supplementary data

Download Word document (2MB)Help with docx files

Electronic Annex: Supplementary Figs. S1 and S2.

References

Appelo and Postma, 2005
C.A.J. Appelo, D. PostmaGeochemistry, Groundwater and Pollution
A.A. Balkema Publishers, Leiden, The Netherlands (2005)
Barth et al., 1989
T. Barth, A.E. Borgund, A.L. HoplandGeneration of organic compounds by hydrous pyrolysis of Kimmeridge oil shale –
bulk results and activation energy calculations
Org. Geochem., 14 (1989), pp. 69-76
ArticleDownload PDFView Record in Scopus
Bell et al., 1994
J.L.S. Bell, D.A. Palmer, H.L. Barnes, S.E. DrummondThermal decomposition of acetate: III. Catalysis by mineral surfaces
Geochim. Cosmochim. Acta, 58 (1994), pp. 4155-4177
ArticleDownload PDFView Record in Scopus
Benson and Cole, 2008
S.M. Benson, D.R. ColeCO2 sequestration in deep sedimentary formations
Elements, 4 (5) (2008), pp. 325-331
CrossRefView Record in Scopus
Bickle, 2009
M.J. BickleGeological carbon storage
Nat. Geosci., 2 (12) (2009), pp. 815-818
CrossRefView Record in Scopus
Burant et al., 2013
A. Burant, G.V. Lowry, A.K. KaramalidisPartitioning behavior of organic contaminants in carbon storage environments: a
critical review
Environ. Sci. Technol., 47 (2013), pp. 37-54

CrossRefView Record in Scopus

Carothers and Karaka, 1978

W.W. Carothers, Y.K. KarakaAliphatic acid anions in oil-field waters – implications for origin of natural gas

AAPG Bull., 62 (12) (1978), pp. 2441-2453

View Record in Scopus

Chen and Bahnemann, 2000

Q.W. Chen, D.W. BahnemannReduction of carbon dioxide by magnetite: implications for primordial synthesis of organic molecules

J. Am. Chem. Soc., 122 (2000), pp. 970-971

CrossRefView Record in Scopus

Chueh and Prausnitz, 1967

P.L. Chueh, J.M. PrausnitzVapor–liquid equilibria at high pressures. Vapor-phase fugacity coefficients in non-polar and quantum-gas mixtures

Ind. Eng. Chem. Fundam., 6 (1967), pp. 492-498

CrossRefView Record in Scopus

de Smit and Weckhuysen, 2008

E. de Smit, B.M. WeckhuysenThe renaissance of iron-based Fischer–Tropsch synthesis: on the multifaceted catalyst deactivation behaviour

Chem. Soc. Rev., 37 (2008), pp. 2758-2781

CrossRefView Record in Scopus

Dictor and Bell, 1986

R.A. Dictor, A.T. BellFischer–Tropsch synthesis over reduced and unreduced iron oxide catalysts

J. Catal., 97 (1986), pp. 121-136

ArticleDownload PDFView Record in Scopus

Drever and Stillings, 1997

J.I. Drever, L.L. StillingsThe role of organic acids in mineral weathering

Colloids Surf., A, 120 (1997), pp. 167-181

ArticleDownload PDFView Record in Scopus

Duan and Sun, 2003

Z.H. Duan, R. SunAn improved model calculating CO_2 solubility in pure water and aqueous NaCl solutions from 273 to 533 K and from 0 to 2000 bar

Chem. Geol., 193 (3–4) (2003), pp. 257-271

ArticleDownload PDFView Record in Scopus

Fu et al., 2007

Q. Fu, B. Sherwood Lollar, J. Horita, G. Lacrampe-Couloume, W.E. Seyfried Jr.Abiotic formation of hydrocarbons under hydrothermal conditions: constraints from chemical and isotopic data

Geochim. Cosmochim. Acta, 71 (2007), pp. 1982-1998

ArticleDownload PDFView Record in Scopus

Ganor et al., 2009

Ganor J., Reznik I. J. and Rosenberg Y. O. (2009) Organics in water–rock interactions. In Thermodynamics and Kinetics of Water–Rock Interaction, vol. 70, pp. 259–369.

Giggenbach, 1987

W.F. GiggenbachRedox processes governing the chemistry of fumarolic gas discharges from White Island, New Zealand

Appl. Geochem., 2 (1987), pp. 143-161

ArticleDownload PDFView Record in Scopus

Gracia et al., 2009

J.M. Gracia, F.F. Prinsloo, J.W. NiemantsverdrietMars-van Krevelen-like mechanism of CO hydrogenation on an iron carbide surface

Catal. Lett., 133 (2009), pp. 257-261

[CrossRef](#)[View Record in Scopus](#)

Grenoble and Estadt, 1981

D.C. Grenoble, M.M. EstadtThe chemistry and catalysis of the water gas shift reaction

J. Catal., 67 (1981), pp. 90-102

[ArticleDownload PDFView Record in Scopus](#)

Haggerty, 1978

S.E. HaggertyThe redox state of planetary basalts

Geophys. Res. Lett., 5 (6) (1978), pp. 443-446

[CrossRefView Record in Scopus](#)

Hartland et al., 2012

A. Hartland, A. Baker, W. Timms, Y. Shutova, D. YuMeasuring dissolved organic carbon $\delta 13C$ in freshwaters using total organic carbon cavity ring-down spectroscopy (TOC-CRDS)

Environ. Chem. Lett., 10 (2012), pp. 309-315

[CrossRefView Record in Scopus](#)

Helgeson et al., 1978

H.C. Helgeson, J.M. Delany, H.W. Nesbitt, D.K. BirdSummary and critique of the thermodynamic properties of rock-forming minerals

Am. J. Sci., 278-A (1978), pp. 1-222

[View Record in Scopus](#)

Helgeson et al., 1993

H.C. Helgeson, A.M. Knox, C.E. Owens, E.L. ShockPetroleum, oil field waters, and authigenic mineral assemblages: are they in metastable equilibrium in hydrocarbon reservoirs?

Geochim. Cosmochim. Acta, 57 (1993), pp. 3295-3339

[ArticleDownload PDFView Record in Scopus](#)

Hitchon, 1996

B. Hitchon (Ed.), Aquifer Disposal of Carbon Dioxide, Geosci. Publ., Sherwood Park, Alberta, Canada (1996)

Horita and Berndt, 1999

J. Horita, M.E. BerndtAbiogenic methane formation and isotopic fractionation under hydrothermal conditions

Science, 285 (1999), pp. 1055-1057

[CrossRefView Record in Scopus](#)

Huo et al., 2009

C.F. Huo, Y.W. Li, J. Wang, H. JiaoInsight into CH4 formation in iron-catalyzed Fischer–Tropsch synthesis

J. Am. Chem. Soc., 131 (2009), pp. 14713-14721

[CrossRefView Record in Scopus](#)

Johnson et al., 2000

Johnson J., Anderson G. and Parkhurst D. (2000) Database from 'thermo.com.V8.R6.230' prepared at L.L.N.L.

Johnson et al., 2004

S.B. Johnson, T.H. Yoon, A.J. Slowey, G.E. BrownAdsorption of organic matter at mineral/water interfaces: 3. Implications of surface dissolution for adsorption of oxalate

Langmuir, 20 (2004), pp. 11480-11492

[CrossRefView Record in Scopus](#)

Johnson et al., 2014

N.C. Johnson, B. Thomas, K. Maher, R.J. Rosenbauer, D. Bird, G.E.Brown Jr.Olivine dissolution and carbonation under conditions relevant for in situ carbon storage
Chem. Geol., 373 (2014), pp. 93-105
ArticleDownload PDFView Record in Scopus
Kelemen and Hirth, 2012
P.B. Kelemen, G. HirthReaction-driven cracking during retrograde metamorphism: olivine hydration and carbonation
Earth Planet. Sci. Lett., 345–348 (2012), pp. 81-89
ArticleDownload PDFView Record in Scopus
Kelemen and Matter, 2008
P.B. Kelemen, J. MatterIn situ carbonation of peridotite for CO2 storage
Proc. Natl. Acad. Sci. USA, 105 (2008), pp. 17295-17300
CrossRefView Record in Scopus
Kharaka et al., 1977
Kharaka Y. K., Callender E. and Carothers W. W. (1977) Geochemistry of geopressured geothermal waters from the Texas Gulf Coast. In Proc. 3rd Geopressured-Geothermal Energy Conf. Univ. Southwestern Louisiana, Lafayette. pp. GI-121–GI-155.
Knauss et al., 1997
K.G. Knauss, S.A. Copenhaver, R.L. Braun, A.K. BurnhamHydrous pyrolysis of New Albany and Phosphoria shales: production kinetics of carboxylic acids and light hydrocarbons and interactions between inorganic and organic chemical systems
Org. Geochem., 27 (1997), pp. 477-496
ArticleDownload PDFView Record in Scopus
Krevor et al., 2012
S.C.M. Krevor, R. Pini, L. Zuo, S.M. BensonRelative permeability and trapping of CO2 and water in sandstone rocks at reservoir conditions
Water Resour. Res., 48 (2012), pp. 1-16
Lawrence et al., 2014
C. Lawrence, J. Harden, K. MaherModeling the influence of organic acids on soil weathering
Geochim. Cosmochim. Acta, 139 (2014), pp. 487-507
ArticleDownload PDFView Record in Scopus
Lu et al., 2012
J. Lu, Y.K. Kharaka, J.J. Thordsen, J. Horita, A. Karamalidis, C. Griffith, J.A.Hakala, G. Ambats, D.R. Cole, T.J. Phelps, M.A. Manning, P.J. Cook, S.D. HovorkaCO2–rock–brine interactions in Lower Tuscaloosa Formation at Cranfield CO2sequestration site, Mississippi, USA
Chem. Geol., 291 (2012), pp. 269-277
ArticleDownload PDFCrossRefView Record in Scopus
Luquot et al., 2012
L. Luquot, M. Andreani, P. Gouze, P. CampsCO2 percolation experiment through chlorite/zeolite-rich sandstone (Pretty Hill Formation – Otway Basin-Australia)
Chem. Geol., 294–295 (2012), pp. 75-88
ArticleDownload PDFView Record in Scopus
Mars et al., 1963
P. Mars, J.J.F. Scholten, P. ZwieteringThe catalytic decomposition of formic acid
Adv. Catal., 14 (1963), pp. 35-113
ArticleDownload PDFView Record in Scopus
Marshall and Medlin, 2011

S.T. Marshall, J.W. MedlinSurface-level mechanistic studies of adsorbate–adsorbate interactions in heterogeneous catalysis by metals
Surf. Sci. Rep., 66 (2011), pp. 173-184
ArticleDownload PDFView Record in Scopus

Mayhew et al., 2013
L.E. Mayhew, E.T. Ellison, T.M. McCollom, T.P. Trainor, A.S. TempletonHydrogen generation from low-temperature water–rock reactions
Nat. Geosci., 6 (2013), pp. 478-484
CrossRefView Record in Scopus

McCollom and Seewald, 2001
T.M. McCollom, J.S. SeewaldA reassessment of the potential for reduction of dissolved CO2 to hydrocarbons during serpentinization of olivine
Geochim. Cosmochim. Acta, 65 (2001), pp. 3769-3778
ArticleDownload PDFView Record in Scopus

McCollom and Seewald, 2003a
T.M. McCollom, J.S. SeewaldExperimental constraints on the hydrothermal reactivity of organic acids and acid anions: I. Formic acid and formate
Geochim. Cosmochim. Acta, 67 (2003), pp. 3625-3644
ArticleDownload PDFView Record in Scopus

McCollom and Seewald, 2003b
T.M. McCollom, J.S. SeewaldExperimental study of the hydrothermal reactivity of organic acids and acid anions: II. Acetic acid, acetate and valeric acid
Geochim. Cosmochim. Acta, 67 (2003), pp. 3645-3664
ArticleDownload PDFView Record in Scopus

McCollom and Seewald, 2006
T.M. McCollom, J.S. SeewaldCarbon isotope composition of organic compounds produced by abiotic synthesis under hydrothermal conditions
Earth Planet. Sci. Lett., 243 (2006), pp. 74-84
ArticleDownload PDFView Record in Scopus

McCollom and Seewald, 2007
T.M. McCollom, J.S. SeewaldAbiotic synthesis of organic compounds in deep-sea hydrothermal environments
Chem. Rev., 107 (2007), pp. 382-401
CrossRefView Record in Scopus

Mohd Amin et al., 2014
S. Mohd Amin, D.J. Weiss, M.J. BluntReactive transport modeling of geologic CO2 sequestration in saline aquifers: the influence of pure CO2 and of mixtures of CO2 and CH4 on the sealing capacity of cap rock at 37 °C and 100 bar
Chem. Geol., 367 (2014), pp. 39-50
ArticleDownload PDFView Record in Scopus

Morin et al., 2009
G. Morin, Y. Wang, G. Ona-Nguema, F. Juillot, G. Calas, N. Menguy, E.Aubry, J.R. Bargar, G.E. Brown Jr.EXAFS and HRTEM evidence for As(III)-containing surface precipitates on nano crystalline magnetite: implications for as sequestration
Langmuir, 25 (2009), pp. 9119-9128
CrossRefView Record in Scopus

Niemantsverdriet and van der Kraan, 1980
J.W. Niemantsverdriet, A.M. van der KraanBehavior of metallic iron catalysts during Fischer–Tropsch synthesis studied with Mössbauer Spectroscopy, X-ray diffraction, carbon content determination, and reaction kinetic mechanisms

J. Phys. Chem., 84 (1980), pp. 3363-3370

CrossRefView Record in Scopus

Ohtomo et al., 2013

Y. Ohtomo, A. Ijiri, Y. Ikegawa, M. Tsutsumi, H. Imachi, G.-I. Uramoto, T.Hoshino, Y. Morono, S. Sakai, Y. Saito, W. Tanikawa, T. Hirose, F. InagakiBiological CO2 conversion to acetate in subsurface coal-sand formation using a high-pressure reactor system

Front. Microbiol., 4 (2013), p. 361

Palmer and Drummond, 1986

D.A. Palmer, S.E. DrummondThermal decarboxylation of acetate. Part I. The kinetics and mechanism of reaction in aqueous solution

Geochim. Cosmochim. Acta, 50 (1986), pp. 813-823

ArticleDownload PDFView Record in Scopus

Peterson et al., 1996

M.L. Peterson, G.E. Brown Jr., G.A. ParksDirect EXAFS evidence for heterogeneous redox reaction at the aqueous chromium/magnetite interface

Colloids Surf., A, 107 (1996), pp. 77-88

ArticleDownload PDFView Record in Scopus

Rosenbauer et al., 2005

R.J. Rosenbauer, T. Koksalan, J.L. PalandriExperimental investigation of CO2–brine–rock interactions at elevated temperature and pressure: implications for CO2 sequestration in deep-saline aquifers

Fuel Process. Technol., 86 (2005), pp. 1581-1597

ArticleDownload PDFView Record in Scopus

Ryan and Reynolds, 1996

P.C. Ryan, R.C. Reynolds Jr.The origin and diagenesis of grain-coating serpentine-chlorite in Tuscaloosa Formation sandstone, U.S. Gulf Coast

Am. Mineral., 81 (1996), pp. 213-225

View Record in Scopus

Schulte and Shock, 1993

M. Schulte, E. ShockAldehydes in hydrothermal solution: standard partial molal thermodynamic properties and relative stabilities at high temperatures and pressures

Geochim. Cosmochim. Acta, 57 (1993), p. 3835

ArticleDownload PDFView Record in Scopus

Schulte and Shock, 2004

M. Schulte, E. ShockCoupled organic synthesis and mineral alteration on meteorite parent bodies

Meteorit. Planet. Sci., 39 (2004), pp. 1577-1590

CrossRefView Record in Scopus

Schulte et al., 2006

M. Schulte, D. Blake, T. Hoehler, T. McCollomSerpentinization and its implications for life on the early Earth and Mars

Astrobiology, 6 (2006), pp. 364-376

CrossRefView Record in Scopus

Seyfried et al., 1979

W.E. Seyfried Jr., P.C. Gordon, F.W. DicksonA new reaction cell for hydrothermal solution equipment

Am. Mineral., 64 (1979), pp. 646-649

View Record in Scopus

Seyfried et al., 1987

W.E. Seyfried, D.R. Janecky, M.E. BerndtRocking autoclaves for hydrothermal experiments, ii. The flexible reaction-cell system

G.C. Ulmer, H.L. Barnes (Eds.), Hydrothermal Experimental Techniques, John Wiley and Sons (1987), pp. 216-239

View Record in Scopus

Shao et al., 2011

H. Shao, J.R. Ray, Y.S. JunEffects of organic ligands on supercritical CO2-induced phlogopite dissolution and secondary mineral formation

Chem. Geol., 290 (2011), pp. 121-132

ArticleDownload PDFView Record in Scopus

Shock, 1988

E.L. ShockOrganic acid metastability in sedimentary basins

Geology, 16 (1988), pp. 886-890

CrossRefView Record in Scopus

Shock, 1990

E.L. ShockGeochemical constraints on the origin of organic compounds in hydrothermal systems

Origins of Life and Evolution of the Biosphere, vol. 20, Kluwer Academic Publishers, Netherlands (1990), pp. 331-367

CrossRefView Record in Scopus

Shock, 1995

E.L. ShockOrganic acids in hydrothermal solutions: standard molal thermodynamic properties of carboxylic acids and estimates of dissociation constants at high temperatures and pressures

Am. J. Sci., 295 (1995), pp. 496-580

CrossRefView Record in Scopus

Shock and Canovas, 2010

E.L. Shock, P. CanovasThe potential for abiotic organic synthesis and biosynthesis at seafloor hydrothermal systems

Geofluids, 10 (1–2) (2010), pp. 161-192

View Record in Scopus

Shock and Helgeson, 1990

E.L. Shock, H.C. HelgesonCalculation of the thermodynamic and transport properties of aqueous species at high pressures and temperatures: standard partial molal properties of organic species

Geochim. Cosmochim. Acta, 54 (1990), pp. 915-945

ArticleDownload PDFView Record in Scopus

Shock and Koretsky, 1993

E.L. Shock, C.M. KoretskyMetal–organic complexes in geochemical processes: calculation of standard partial molal thermodynamic properties of aqueous acetate complexes at high pressures and temperatures

Geochim. Cosmochim. Acta, 57 (1993), pp. 4899-4922

ArticleDownload PDFView Record in Scopus

Shock and Schulte, 1998

E. Shock, M. SchulteOrganic synthesis during fluid mixing in hydrothermal systems

J. Geophys. Res., 103 (1998), pp. 28513-28527

CrossRefView Record in Scopus

Shock et al., 2013

E.L. Shock, P. Canovas, Z. Yang, G. Boyer, K. Johnson, K. Robinson, K.Fecteau, T. Windman, A. CoxThermodynamics of organic transformations in hydrothermal fluids

Rev. Mineral. Geochem., 76 (2013), pp. 311-350

CrossRefView Record in Scopus

Steefel, 2001

Steefel C. I. (2001) Software for modeling multicomponent, multidimensional reactive transport. UCRL-MA-143182. Lawrence Livermore National Laboratory, Livermore, CA.

Steefel and Lasaga, 1994

C.I. Steefel, A.C. LasagaA coupled model for transport of multiple chemical-species and kinetic precipitation dissolution reactions with application to reactive flow in single-phase hydrothermal systems

Am. J. Sci., 294 (1994), pp. 529-592

CrossRefView Record in Scopus

Steefel et al., 2014

C.I. Steefel, C.A.J. Appelo, B. Arora, D. Jacques, T. Kalbacher, O. Kolditz, V. Lagneau, P.C. Lichtner, K.U. Mayer, J.C.L. Meeussen, S. Molins, D. Moulton, H.Shao, J. Šimůnek, N. Spycher, S.B. Yabusaki, G.T. YehReactive transport codes for subsurface environmental simulation

Comp. Geo. (2014), 10.1007/s10596-014-9443-x.i

Stillings et al., 1996

L.L. Stillings, J.I. Drever, S.L. Brantley, Y.T. Sun, R. OxburghRates of feldspar dissolution at pH 3–7 with 0–8 mM oxalic acid

Chem. Geol., 132 (1996), pp. 79-89

ArticleDownload PDFView Record in Scopus

Thüne et al., 2012

P. Thüne, P. Moodley, F. Scheijen, H. Fredriksson, R. Lancee, J. Kropf, J.Miller, J.W. Nie- mantsverdrietThe effect of water on the stability of iron oxide and iron carbide nano particles in hydrogen and syngas followed by in situ X-ray absorption spectroscopy

J. Phys. Chem. C, 116 (2012), pp. 7367-7373

CrossRefView Record in Scopus

Van Der Laan and Beenackers, 1999

G.P. Van Der Laan, A.A.C.M. BeenackersKinetics and selectivity of the Fischer–Tropsch synthesis: a literature review

Catal. Rev., 41 (1999), pp. 255-318

CrossRefView Record in Scopus

Watson et al., 2004

M. Watson, N. Zwingman, N. LemonThe Ladbroke Grove–Katnook carbon dioxide natural laboratory: a recent CO2accumulation in a lithic sandstone reservoir

Energy, 29 (9) (2004), pp. 1457-1466

ArticleDownload PDFView Record in Scopus

White et al., 1994

A.F. White, M.L. Peterson, M.F. Hochella Jr.Electrochemistry and dissolution kinetics of magnetite and ilmenite

Geochim. Cosmochim. Acta, 58 (8) (1994), pp. 1859-1875

ArticleDownload PDFView Record in Scopus

Williams et al., 2011

L.B. Williams, J.R. Holloway, B. Canfield, C.R. Glein, J.M. Dick, H.E.Hartnett, E.L. ShockBirth of biomolecules from the warm wet sheets of clays near spreading centers

S. Golding, M. Glikson (Eds.), Earliest Life on Earth, Environments and Methods of Detection, Springer, New York (2011)

Xu et al., 2004

T. Xu, J.A. Apps, K. PruessReactive geochemical transport simulation to study mineral trapping for CO2disposal in deep arenaceous formations

J. Geophys. Res., 108 (2004), pp. 1-13

CrossRefView Record in Scopus

Zhuo et al., 2009

M. Zhuo, K.F. Tan, A. Borgna, M. SaeysDensity functional theory study of the CO insertion mechanism for Fischer–Tropsch synthesis over CO catalysts

J. Phys. Chem. C, 113 (2009), pp. 8357-8365

CrossRefView Record in Scopus